Direct numerical simulation of transition in a sharp cone boundary layer at Mach 6: fundamental breakdown

Jayahar Sivasubramanian[1],† and Hermann F. Fasel[1]

[1]Department of Aerospace and Mechanical Engineering, University of Arizona, Tucson, AZ 85721, USA

Direct numerical simulations (DNS) were performed to investigate the laminar–turbulent transition in a boundary layer on a sharp cone with an isothermal wall at Mach 6 and at zero angle of attack. The motivation for this research is to make a contribution towards understanding the nonlinear stages of transition and the final breakdown to turbulence in hypersonic boundary layers. In particular, the role of second-mode fundamental resonance, or (K-type) breakdown, is investigated using high-resolution 'controlled' transition simulations. The simulations were carried out for the laboratory conditions of the hypersonic transition experiments conducted at Purdue University. First, several low-resolution simulations were carried out to explore the parameter space for fundamental resonance in order to identify the cases that result in strong nonlinear interactions. Subsequently, based on the results from this study, a set of highly resolved simulations that proceed deep into the turbulent breakdown region have been performed. The nonlinear interactions observed during the breakdown process are discussed in detail in this paper. A detailed description of the flow structures that arise due to these nonlinear interactions is provided and an analysis of the skin friction and heat transfer development during the breakdown is presented. The controlled transition simulations clearly demonstrate that fundamental breakdown may indeed be a viable path to complete breakdown to turbulence in hypersonic cone boundary layers at Mach 6.

Key words: boundary layer stability, high-speed flow, transition to turbulence

1. Introduction

Hypersonic flow is physically different from low-speed flow, characterized by physical phenomena that become relevant only at high Mach numbers. For example, the enormous aerodynamic heating imposed on the structure of flight vehicles represents one of the main difficulties in the design and safe operation of hypersonic vehicles (Haney 1983). At large Reynolds numbers, the boundary layer can be turbulent and the aero-thermal loads are much increased compared to laminar flow. Therefore, laminar–turbulent boundary layer transition has an important design implication, especially also for the design of the thermal protection system (TPS).

† Email address for correspondence: jayahar@email.arizona.edu

Due to the lack of reliable transition prediction tools for hypersonic flows, engineers have used a rather conservative approach for designing the TPS, for example, by assuming the boundary layers to be turbulent over the entire surface (see Berry, Hamilton & Wurster 2006; Berry & Horvarth 2008). This conservative approach results in an overly heavy and expensive TPS, thus reducing the range and/or payload of hypersonic vehicles. Therefore, accurate estimates of the transition location are of vital importance for the design of future hypersonic vehicles, because only then can the aero-thermal loads and surface temperatures be adequately predicted. A TPS design based upon the improved understanding of hypersonic transition, together with reduced design margins, will ultimately lead to enhanced payload capabilities in the next generation of hypersonic vehicles (e.g. next generation reusable launch vehicles (RLV) or space access vehicles).

Transition to turbulence in hypersonic boundary layers is a major unresolved topic in fluid dynamics. Even after many years of research, crucial aspects of the transition physics are still unknown. This may be attributed in part to the increased complexity of the physics when compared to transition in subsonic boundary layers (see Balakumar & Malik 1992; Tumin 2007; Fedorov 2011). From linear stability theory (LST) (Mack 1969, 1975, 1984), it is known that multiple instability modes exist for high-speed boundary layer flows, in contrast to only one mode (Tollmien–Schlichting, TS) for the subsonic or incompressible case. In addition to the so-called first mode in supersonic/hypersonic boundary layers, higher modes exist for supersonic/hypersonic boundary layers that result from an inviscid instability mechanism. According to LST, for Mach 6 the most unstable of the higher modes is the second mode. In contrast to the first modes, which have the highest amplification rates for oblique waves, the second modes have the highest amplification for two-dimensional or axisymmetric waves. Also from LST, it is known that the first mode is dominant (higher amplification rates) for low supersonic Mach numbers while for Mach numbers above 4 (hypersonic boundary layers) the second mode is dominant. Due to the difficulties in carrying out hypersonic boundary layer experiments ('controlled' experiments, in particular) and due to the existence of multiple instability modes, the role and importance of the various instability modes in a realistic transition process are not understood at all (see Schneider 2001, 2004). Of course, when amplitudes of the various instability modes reach high enough levels, nonlinear interactions of these modes can occur. As a consequence, the transition process in hypersonic boundary layers is highly non-unique, which means that slight changes in the disturbance environment or vehicle geometry may significantly alter the transition process.

Direct numerical simulations (DNS) that capture part or all of the transition region in hypersonic boundary layers, on the other hand, require very high grid resolution and are therefore computationally very expensive. As a consequence, most of the earlier experimental and numerical efforts have focused on the linear receptivity (e.g. Maslov *et al.* 2001; Zhong 2001) process and the linear regime of boundary layer transition (e.g. Demetriades 1960, 1977). Relatively little is known about the late nonlinear stages of transition and, in particular, about the final breakdown to turbulence. Due to the stabilizing effect of compressibility, the nonlinear transition regime can cover a significant downstream extent of a hypersonic flight vehicle. As a result, transition prediction tools based on the linear N-factor calculations cannot estimate the actual transition 'location' accurately. Therefore, new transition prediction tools, which also incorporate nonlinear transition physics, are crucially needed for the development and safe operation of future high-speed flight vehicles.

Hence, it is very important to understand the nonlinear stages of transition, including the final breakdown to turbulence, in order to identify which nonlinear mechanisms lead to fully turbulent flow and which do not. Therefore, accurate and reliable fully resolved DNS of hypersonic boundary layer transition are essential for advancing our understanding of hypersonic transition and for developing reliable transition prediction tools.

Cones with circular cross-section represent a useful prototypical geometry for investigating boundary layer stability and transition at high speeds (Schneider 2004). In fact, in many of the modern high-speed applications, the nose region of the flight vehicle can be approximated as some sort of a cone. Boundary layer stability investigations have been carried out for sharp cones since the 1970s (earlier hypersonic measurements were for flat plates, Schneider 2004). Demetriades (1974, 1978) measured second-mode instabilities for 4° and 5° half-angle cones at Mach 8 using hot wires. Kendall (1975) also made hot-wire measurements of instabilities for a 4° half-angle cone at Mach 8.5 and compared amplification rates with theory. Both measurements and theory showed a dominance of the second-mode instability waves. Among the early research efforts, the most detailed experiments on hypersonic boundary layers on a circular cone are those of Stetson and co-workers (Stetson *et al.* 1983, 1984, 1985, 1986, 1989; Stetson & Kimmel 1992, 1993) for a 7° half-angle cone at Mach 8. They have investigated the influence of nose radius, unit Reynolds number, and transverse curvature for a cone boundary layer at Mach 8 in a conventional 'noisy' wind tunnel. They made detailed hot-wire measurements and in all cases they found that the two-dimensional or axisymmetric second-mode waves were the dominant instability waves. In their experiments streamwise amplified second-harmonics were observed which is an indication of the presence of nonlinear effects.

However, from these experiments it was still not clear what role the second-mode waves play in the nonlinear stages of the transition process. Another major effort was carried out at NASA Langley in the Mach 6 quiet tunnel (Lachowicz, Chokani & Wilkinson 1996). In recent experiments, Maslov and co-workers (Bountin, Shiplyuk & Sidorenko 1999; Shiplyuk *et al.* 2003; Maslov *et al.* 2006; Bountin, Shiplyuk & Maslov 2008) investigated transition in a sharp cone boundary layer at Mach 6 in a conventional tunnel. They perturbed the boundary layer using a glow discharge actuator as a harmonic point source. Using the bi-coherence spectrum method (see Chokani 1999, 2005) they concluded that the basic mechanism of nonlinear interaction at the location of the maximum root-mean-square (r.m.s.) voltage fluctuation in a Mach 6 cone boundary layer was a subharmonic resonance. However, poor spatial and temporal resolution in the experimental data had made it difficult to confirm their results. In those experiments, the nonlinear wave interactions are typically studied by performing statistical analysis of the disturbance spectrum obtained at several streamwise locations along the same azimuthal plane, e.g. the centreline plane (see for example, Shiplyuk *et al.* 2003; Bountin *et al.* 2008). Hence, data are available only for the frequency interactions and it is very difficult to identify the spanwise or azimuthal modes involved in the nonlinear interactions.

Some of the first linear stability calculations for a cone boundary layer were conducted by Malik (1984), Gasperas (1987) and Mack (1987). Malik (1984) investigated a boundary layer on a sharp cone (5° half-angle) at zero angle of attack for several supersonic Mach numbers. He did not consider the curvature terms for the calculation of the mean-flow profiles and for the eigenvalue analysis. The mean-flow conditions used in his calculations matched the flight experiments from Fisher &

Dougherty ([1982](#)) (Mach 1.2, 1.35, 1.6 and 1.92) and the quiet tunnel experiments by Beckwith *et al.* ([1983](#)) for Mach 3.5 (before shock). Malik ([1984](#)) showed that in these low-free-stream disturbance experiments, transition could be predicted by the e^N method with N ranging from 9 to 11. This was confirmed by the experimental and numerical studies by Chen, Malik & Beckwith ([1988](#), [1989](#)) for a sharp cone and a flat plate at Mach 3.5. Gasperas ([1987](#)) and Mack ([1987](#)) investigated the linear stability behaviour of disturbances in hypersonic boundary layers on sharp cones at Mach 8 and compared their results to the Stetson experiments (Stetson *et al.* [1983](#)). Results of Gasperas ([1987](#)) and Mack ([1987](#)) obtained from LST did not agree well with the experiments. This is probably due to the nonlinear effects in the experiments since Stetson *et al.* ([1983](#)) used a conventional 'noisy' wind tunnel. However, the experimental results confirmed that two-dimensional or axisymmetric instability waves (second-mode waves) are the most unstable disturbances at Mach 8 (Mack [1987](#)).

Many numerical investigations have focused on the nonlinear transition regime of high-speed boundary layers. For example, Eissler ([1995](#)) performed simulations for a boundary layer at Mach 4.8 under wind tunnel (so-called 'cold') conditions and free-flight (so-called 'hot') conditions using a radiation-cooled wall model in an attempt to estimate realistic heat fluxes on the wall during transition. His simulations with an adiabatic and radiation-cooled wall revealed that the so-called oblique breakdown (see for example Thumm [1991](#); Fasel, Thumm & Bestek [1993](#); Eissler & Bestek [1996](#)) is the strongest nonlinear mechanism for wind tunnel ('cold') conditions at Mach 4.8. Under atmospheric ('hot') conditions, secondary three-dimensional waves of a fundamental (K-type) breakdown (see Herbert [1988](#); Kachanov [1994](#)) showed significant amplitude levels only far downstream and a subharmonic resonance (N-/H-type) could not be found. Due to limited computer resources available at that time, Eissler ([1995](#)) was not able to perform K-type and N-/H-type breakdown simulations for an isothermal wall. Several numerical investigations using DNS and PSE have addressed the transition problem for the flow conditions of the Stetson Mach 8 experiments (Stetson *et al.* [1983](#)). Pruett & Chang ([1995](#)) and Pruett *et al.* ([1995](#)) investigated several transition routes and found that subharmonic resonances (N-/H-type) are an unlikely path to turbulence since the downstream extent of the instability region of two-dimensional or axisymmetric waves is too short. Instead, they conjectured that a second-mode oblique breakdown was responsible for transition in the Stetson experiments. The steady vortices arising due to nonlinear interactions were found to have a significant impact on the stability behaviour. Later, Fezer & Kloker ([2001](#)) and more recently Husmeier & Fasel ([2007](#)) performed numerical simulations to indentify the relevant breakdown mechanisms. Despite the considerable progress that has been made towards building a fundamental understanding of the nonlinear transition regime of hypersonic cone boundary layers many questions remain.

Most of the experimental and numerical investigations that addressed the nonlinear transition regime for high-speed boundary layers (also discussed above) have focused on particular transition scenarios, where the flow is perturbed with only a limited number of waves ('controlled' scenario). However, in a natural 'uncontrolled' scenario, the perturbation is composed of a large number of waves and therefore numerous possibilities of nonlinear interactions exist. Hence, controlled transition can only provide limited insight into the natural transition scenario. Therefore, in our previous research we explored which nonlinear mechanisms may be dominant in a broad-band disturbance environment for a sharp cone boundary layer at Mach 6. Towards this end, a 'natural transition' scenario was modelled and investigated using wavepacket disturbances, which were generated by a short-duration (localized) blowing and

Flow parameters

Approach flow		Boundary layer edge	
Re/L (m^{-1})	10.5×10^6	Re_e/L (m^{-1})	13.6×10^6
M (—)	6.0	M_e (—)	5.35
T_0^* (K)	430.0	T_e^* (K)	63.92
p_0^* (kPa)	1043.0		

TABLE 1. Flow parameters used in the simulations presented in this paper (based on the approach flow conditions in the cone experiments conducted in the Boeing/AFOSR Mach 6 quiet-flow tunnel at Purdue University (Casper *et al.* 2009; Alba *et al.* 2010)).

suction pulse (see Sivasubramanian *et al.* 2009; Sivasubramanian & Fasel 2010, 2012*a*, 2014). The three-dimensional wavepacket consists of a wide range of disturbance frequencies and wavenumbers. Several DNS were performed for a hypersonic cone boundary layer at Mach 6 with varying pulse amplitudes. First, using a low-amplitude pulse the linear development of a wavepacket was investigated. The amplitude of the pulse was then increased to investigate the nonlinear effects. These wavepacket simulations provided strong evidence for the presence of a second-mode fundamental and oblique breakdown mechanism. In addition, the wavepacket simulations have also indicated a possible presence of a subharmonic resonance mechanism.

Due to the broad-band forcing of multiple frequencies and wavenumbers in the wavepacket simulations, the nonlinear interactions between different wave components are highly complex. Therefore, in order to determine which of these nonlinear mechanisms were most relevant for the entire transition process, that is, determine which of these mechanisms can indeed lead to a complete breakdown to turbulence and to fully developed turbulent flow, it is necessary to perform simulations where the initial number of possible nonlinear interactions is limited. Towards this end, controlled transition simulations were performed where only a few specified modes are forced. In particular, in the present paper the second-mode fundamental breakdown mechanism is investigated for a cone boundary layer at Mach 6. An overview of the computational set-up for the DNS is provided and discussed in §2. In §4, results from several DNS are discussed. It is shown in detail how the fundamental secondary instability develops, from the onset all the way through the late stages of transition and into turbulence.

2. Physical problem and computational approach

The computational set-up is based on the experiments conducted in the Boeing/ AFOSR Mach 6 quiet-flow Ludwieg Tube at Purdue University by Schneider and co-workers (Casper *et al.* 2009; Alba *et al.* 2010). The cone model used in the Purdue experiments (see figure 1) has a half vertex angle of 7° and a cone length $L^* = 0.517$ m. The nose radius of the cone is $r_{nose}^* = 0.05$ mm and, therefore, the cone can be considered a 'sharp cone'. The approach flow has a Mach number of 6 and a unit Reynolds number of 10.5×10^6 m^{-1}. The stagnation temperature and pressure are 430 K and 1043 kPa, respectively (see Casper *et al.* 2009; Alba *et al.* 2010). A summary of the flow parameters of the Purdue experiments is provided in table 1. A schematic of the cone model with the computational domain and the boundary conditions is shown in figure 2. The computational domain starts at $x_0^* = 0.112$ m and, thus, does not include the nose tip. The outflow boundary is located at $x_L^* = 0.6$ m.

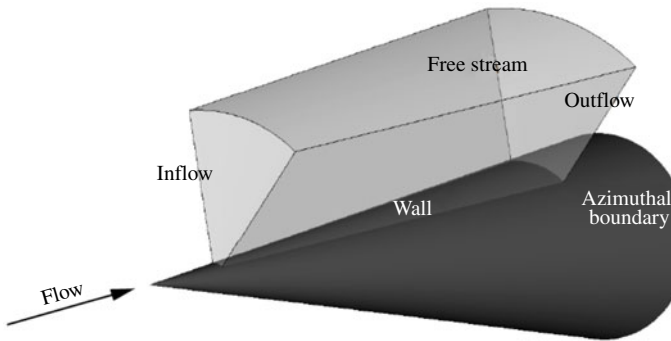FIGURE 1. Cone model used in the Purdue experiments (S. P. Schneider 2009, private communication).

FIGURE 2. Cone model with the computational domain and boundary conditions. The 'sharp' cone has a nose radius of 0.05 mm and a semi vertex angle of $7°$.

A domain longer than the experimental cone model is used in the simulations in order to accommodate a computational buffer domain. The buffer domain starts at $x^* = 0.58$ m. The domain height was chosen to be $y_H^* = 0.123$ m. The main simulation parameters used for the results presented in this paper are provided in table 2.

2.1. *Simulation strategy and initial condition*

The simulation strategy for the simulations presented consists of three steps (see figure 3). First, in a precursor calculation (step 1), using a finite-volume code developed in our CFD laboratory by Gross & Fasel (2008, 2010), the steady undisturbed basic flow around the entire axisymmetric cone geometry is computed using a second-order-accurate discretization (see figure 3). Due to the low-order accuracy this code is too diffusive to directly perform stability and transition simulations with a reasonable number of grid points. Therefore, in the second step, the steady basic flow obtained by the precursor calculation is used as an initial condition for calculating a highly accurate basic flow using the high-order-accurate finite-difference code, which was also developed in our laboratory by Laible, Mayer & Fasel (2008, 2009). The computational domain (see figure 3) for the high-order-accurate basic flow computation (in step 2) does not cover the entire flow

	Linear (low-amplitude) simulations	Parameter study	High-resolution simulations
Domain size			
x_0^* (m)	0.112	0.112	0.112
x_L^* (m)	0.6	0.6	0.6
y_H^* (m)	0.123	0.123	0.123
k_c (cone section) (—)	0	60–130	100
Forcing location			
x_1^* (m)	0.136	0.136	0.136
x_2^* (m)	0.140	0.140	0.140
Grid size (number of points)			
n_x (—)	1821	2391	6421
n_y (—)	300	300	300
K (modes in z) (—)	1	5	48–128
n_z (—)	1	9	95–255
Grid resolution			
Δt (—)	4.1483×10^{-6}	4.1483×10^{-6}	4.1483×10^{-6}
Δx^* (inflow) (m)	2.67×10^{-4}	2.69×10^{-4}	2.69×10^{-4}
Δx^* (outflow) (m)	2.67×10^{-4}	1.79×10^{-4}	5.39×10^{-5}
Δy^* (wall) (m)	4.1282×10^{-6}	4.1282×10^{-6}	4.1282×10^{-6}

TABLE 2. Main simulation parameters for the results presented in this paper.

around the cone because it is beneficial to focus all computational resources into the region of interest, i.e. by starting the computational domain downstream of the nose tip. Thus, in the high-order-accurate finite-difference code, the nose tip is not included. However, the oblique shock emanating from the nose tip is included by placing the free-stream boundary above the shock (see § 2.3). The basic flow (initialized using the precursor results) has to be converged again, since the underlying numerical schemes of the finite-volume code and the high-order-accurate finite-difference code have different truncation errors. Finally, in the third step, the newly converged basic flow serves as an initial undisturbed state for the unsteady simulations with a specified disturbance input (see § 3) using the same high-order-accurate code. In the following only the high-order-accurate finite-difference code used for steps 2 and 3 will be discussed. For details regarding the finite-volume code used in step 1, see Gross & Fasel (2008, 2010).

For stability and transition investigations it is imperative to have an accurate undisturbed basic (undisturbed) flow field. For validation purposes, in figures 4 and 5, the streamwise velocity and temperature profiles obtained from the precursor calculation using the finite-volume code and the high-order-accurate finite-difference code are compared to Mangler-transformed (Mangler 1948) profiles calculated from a flat-plate similarity profile. The profiles, plotted here for four different streamwise locations, show excellent agreement. Note that the finite-volume code used for the precursor calculation predicts the boundary layer profiles accurately and provides a high quality initial condition for the simulations performed using the high-order finite-difference code.
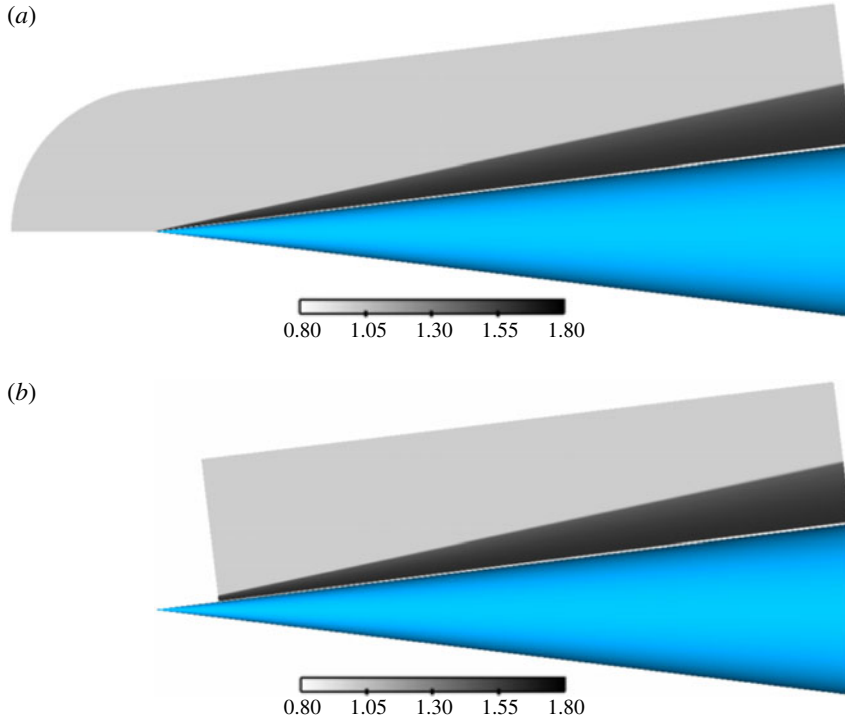
(*a*)

0.80   1.05   1.30   1.55   1.80

(*b*)

0.80   1.05   1.30   1.55   1.80

FIGURE 3. (Colour online) Schematic of the strategy used for the simulations: (*a*)
precursor calculation; (*b*) high-order-accuracy DNS. Note that the computational domain
for the high-order simulation does not cover the entire flow. The contours shown here are
for density

2.2. *Numerical method*

The details of the high-order-accurate finite-difference code used here, along with
its continuing development, have been described in Laible *et al.* (2008, 2009),
Sivasubramanian *et al.* (2009), Sivasubramanian & Fasel (2010, 2011) and Laible
(2011). Therefore, only a short overview will be given here. The numerical method
is based on the three-dimensional Navier–Stokes equations, the continuity equation
and the energy equation for compressible flows in conical coordinates. For the
full set of governing equations in conical coordinates the reader is referred to e.g.
Sivasubramanian & Fasel (2012*b*). The so-called 'spatial model' is employed, so that
the disturbance waves can grow or decay in the downstream direction. This is in
contrast to the so-called 'temporal model', where the disturbances grow in time. For
a detailed discussion of the spatial versus temporal model for stability and transition
investigation see Fasel (1990).

The governing equations are integrated in time using the standard explicit
fourth-order Runge–Kutta method (Ferziger 1998). The spatial discretization is
mainly based on high-order-accurate standard central finite differences. In particular,
sixth-order central finite differences were used in the streamwise direction and
fourth-order central finite differences were used in the wall-normal direction to
discretize the derivatives of the viscous terms and the source term. The inviscid
fluxes are separated into an upwind flux and a downwind flux using van Leer's
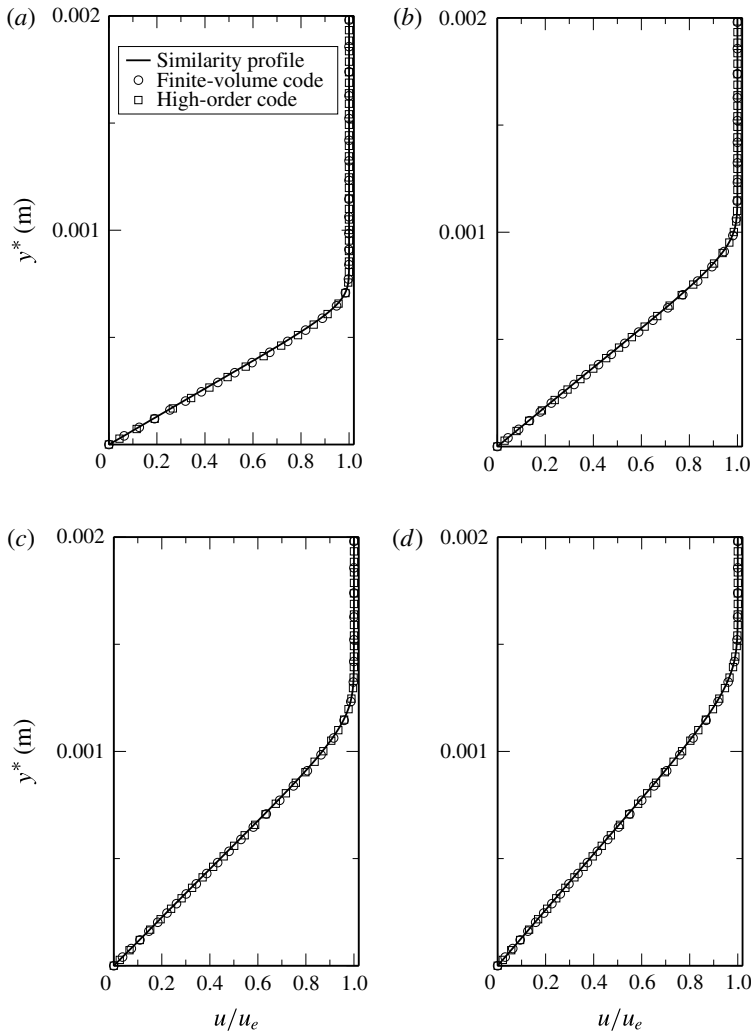splitting (van Leer 1982). Then, grid-centred upwind differences (Zhong 1998) with
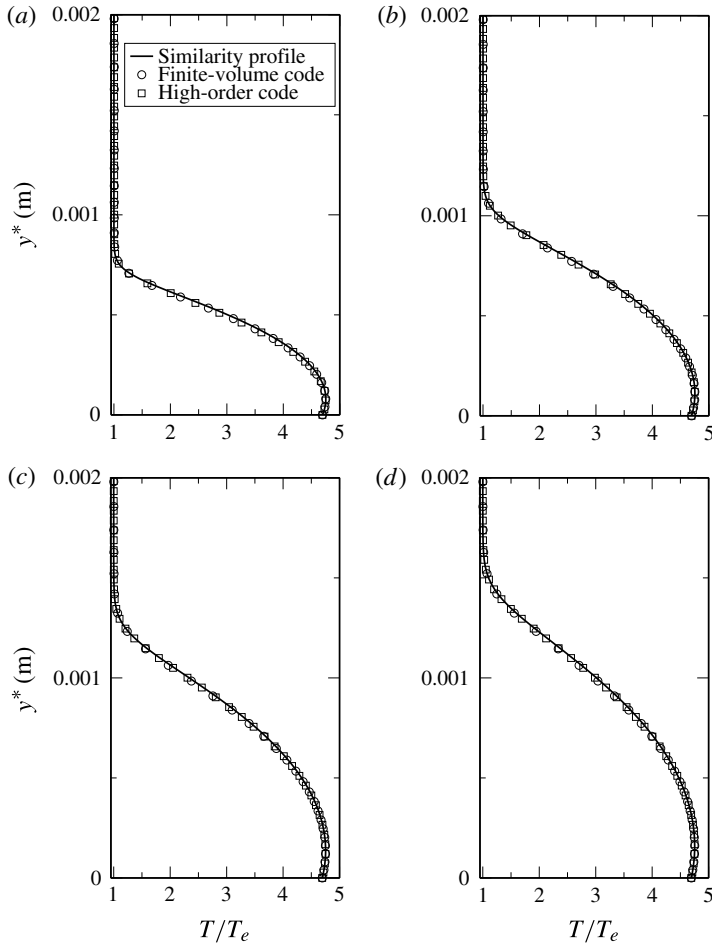
FIGURE 4. Comparison of streamwise velocity profiles computed by the precursor finite-volume code, the high-order code and the Mangler-transformed flat-plate similarity profile at several streamwise locations: (*a*) $x^* = 0.100$ m; (*b*) $x^* = 0.200$ m; (*c*) $x^* = 0.300$ m and (*d*) $x^* = 0.400$ m.

ninth-order accuracy are applied to evaluate the derivatives for these fluxes. In the azimuthal direction, a pseudo-spectral discretization using fast Fourier transforms is employed. Since high-order-accurate boundary closures may develop oscillations and, hence, are usually unstable, special attention was given to the wall-next boundary stencils. The present code employs a method suggested by Zhong & Tatineni (2003). For further details see Laible (2011).

Note that if the high-order-accurate finite differences as described above were used for the calculation of the shock, strong oscillations would be introduced into the computational domain. Therefore, before the simulation, the shock position is detected using the smoothness estimater for the pressure as suggested by Balsara & Shu (2000). Also the order of accuracy of the wall-normal upwind-difference stencils

FIGURE 5. Comparison of temperature profiles computed by the precursor finite-volume code, the high-order code and the Mangler-transformed flat-plate similarity profile at several streamwise locations: (*a*) $x^* = 0.100$ m; (*b*) $x^* = 0.200$ m; (*c*) $x^* = 0.300$ m and (*d*) $x^* = 0.400$ m.

is decreased from ninth-order to first-order in the near-shock region in order to avoid numerical oscillations. Since the shock is multiple boundary layer thicknesses away from the wall and the gradients in the inviscid region are rather small, the higher truncation error of the first-order stencils has no significant effect on the overall accuracy of the scheme and the results. Hence, the instability modes are also not affected by the inclusion of the shock.

2.3. *Boundary conditions*

The inflow (see figure 2) for hypersonic boundary layer simulations is separated into two regions: a subsonic region ($M < 1$) close to the wall and a supersonic/hypersonic region ($M > 1$) away from the wall. In the supersonic/hypersonic region, Dirichlet conditions for u, v, w, T, p and ρ are specified (obtained in our case from a precursor calculation, see §2.1). For the subsonic region in the boundary layer,

a special treatment is occasionally necessary for some applications to avoid undesired reflections, e.g. non-reflecting boundary condition are used as suggested by Poinsot & Lele (1992). However, for the simulations presented here, there was no evidence of reflections at the inflow boundary, even when the Dirichlet conditions were also applied for the subsonic region. Therefore, for the simulations presented in this paper, Dirichlet conditions were prescribed at the inflow over the entire domain height. On the cone surface, no-penetration ($v = 0$) and no-slip ($u = 0$; $w = 0$) conditions were enforced. The wall is set to be isothermal with $T_w^* = 300$ K for the steady base-flow calculations. The wall temperature $T_w^* = 300$ K is slightly lower than the laminar recovery temperature. For the unsteady simulations the temperature fluctuations were set to zero at the wall. The value of the pressure at the wall boundary is obtained from the y-momentum equation. Finally, the density at the wall is computed using the equation of state. At the outflow boundary, the second derivatives of the primitive variables u, v, w, T, and p are set to zero: $\partial^2 u/\partial x^2 = 0$, $\partial^2 v/\partial x^2 = 0$, $\partial^2 w/\partial x^2 = 0$, $\partial^2 T/\partial x^2 = 0$, $\partial^2 p/\partial x^2 = 0$. The density was then determined from the temperature and the pressure by using the equation of state. For simulations of the nonlinear breakdown a buffer domain technique is applied, where finite-amplitude disturbances are ramped down to zero at the outflow (see Meitz & Fasel 2000). Since for all simulations presented here the free stream is located above the oblique shock emanating from the nose of the cone, Dirichlet conditions (u, v, w, T, p, ρ prescribed) can be prescribed at this boundary.

In the azimuthal direction a pseudo-spectral approach with Fourier modes (Canuto *et al.* 1988) was used to calculate the derivatives. In order to save computational resources, symmetric transformations (cosine) are considered for all variables except the azimuthal velocity component, for which anti-symmetric (sine) transformations are used. The adoption of the symmetric and anti-symmetric transformations automatically enforces symmetry conditions on the azimuthal boundaries. Therefore, the azimuthal domain contains only half of the azimuthal wavelength of the primary wave for the fundamental breakdown simulations presented in this paper.

3. Disturbance generation

In the controlled transition simulations presented in this paper, the disturbances are introduced into the flow by time-harmonic wall-normal blowing and suction through a disturbance slot near the upstream end of the computational domain. The no-penetration boundary condition for the wall-normal velocity component is replaced at the blowing and suction slot by

$$v(x, y = 0, \varphi, t) = A_{\omega, k_c} v_p(x_p) \cos(k_c \varphi) \sin(\omega t), \tag{3.1}$$

where A_{ω, k_c}, ω and k_c denote the amplitude, frequency and azimuthal wavenumber of a disturbance. The dimensionless coordinate x_p is defined over the slot width ($x_1 \leqslant x \leqslant x_2$) by

$$x_p = \frac{2x - (x_2 + x_1)}{x_2 - x_1} \tag{3.2}$$

where $x_1^* = 0.136$ m and $x_2^* = 0.140$ m.

The wall-normal velocity disturbance distribution (v_p) in the streamwise direction represents a dipole modelled by a fifth-order polynomial, which is smooth everywhere including the endpoints (Harris 1997) and is shown schematically in figure 6.
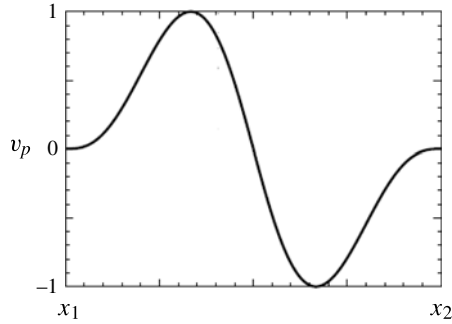
FIGURE 6. Schematic of the streamwise wall-normal disturbance velocity distribution over the forcing slot used for introducing controlled disturbances.

4. Results and discussion

The role of second-mode fundamental (K-type) breakdown and its viability to lead to a complete breakdown to turbulence is investigated for a hypersonic cone boundary layer at Mach 6. Towards this end, controlled transition investigations were carried out using high-fidelity DNS. In these simulations, only a few specified waves or modes are forced. For example, to explore the role of the 'classical' fundamental breakdown (K-type), only three modes are forced, i.e. a primary axisymmetric wave with a high amplitude and a pair of oblique waves with very small amplitudes. First the linear instability regime was studied using LST and DNS. Then, the parameter space was explored using several low-resolution simulations, to identify the cases that result in the strongest nonlinear interactions and thus lead to the most rapid breakdown to turbulence. Then, based on the results of this parameter study, highly resolved simulations that proceed deep into turbulent breakdown region have been performed. The major results from all these simulations are presented and discussed in the following.

4.1. *Linear regime*

The linear transition regime is studied using both LST and DNS. While in a DNS the complete set of nonlinear governing equations is solved without any simplification, in LST these equations are linearized assuming very small disturbance amplitudes. Furthermore, in LST it is assumed that disturbances ϕ' follow the wave ansatz

$$\phi' = \hat{\phi}(y)\, e^{i(\alpha x + \beta z - \omega t)}. \tag{4.1}$$

The complex eigenfunction $\hat{\phi}$ is only dependent on the wall-normal direction y. For the spatial model considered here, α is complex, while β and ω are real. The wave angle of a wave with respect to the streamwise direction is given by

$$\psi = \arctan\left(\frac{\beta}{\alpha_r}\right), \tag{4.2}$$

where

$$\alpha_r = \frac{2\pi}{\lambda_x} \quad \text{and} \quad \beta = \frac{2\pi}{\lambda_z} \tag{4.3a,b}$$

are the streamwise and spanwise (or azimuthal) wavenumbers, respectively. The streamwise wavenumber α_r is the real part of the complex streamwise wavenumber α in (4.1) ($\alpha = \alpha_r + i\alpha_i$), and ω is the angular frequency. For negative values of α_i, disturbances are amplified in the streamwise direction whereas for positive values they are damped. The wave ansatz from (4.1) with the appropriate boundary conditions reduces the linear system of partial differential equations to an eighth-order system of ordinary differential equations, which in fact reduces to an eigenvalue problem, which can be solved efficiently.

For the cone geometry, the decreasing spanwise curvature and the decreasing wave angle of the disturbances as they travel downstream play an important role in both the linear and nonlinear development of the transition process. The decreasing wave angle is a consequence of the body divergence due to the cone geometry, which causes the azimuthal wavelength of a specific wave to increase in the downstream direction. The azimuthal wavelength at the streamwise position x is defined as

$$\lambda_z(x) = \frac{2\pi r(x)}{k_c}. \tag{4.4}$$

The cone radius r is a function of the streamwise direction x and k_c represents the azimuthal mode number. Here the assumption is made that the ratio of the boundary layer thickness and the cone radius is small and that the azimuthal wavelength is equal to the arc length on the cone surface. In this paper, a specific wave is defined by its azimuthal mode number, k_c, and a certain reduced frequency, F. For example, a wave with azimuthal mode number $k_c = 1$ has an azimuthal wavelength equal to the circumference of the cone cross-section, a wave with azimuthal mode number $k_c = 2$ has an azimuthal wavelength of half the circumference, etc. Note that for a cone the azimuthal mode number, k_c, has to be an integer and consequently only a discrete set of physically possible azimuthal wavelengths can exist. This is in contrast to a flat plate for which the spanwise wavelength can take on any value in a continuous fashion. The non-dimensional frequency, F, and the local Reynolds number, R_x, are defined as

$$F = 2\pi \frac{f^* \nu_e^*}{U_e^{*2}} \quad \text{and} \quad R_x = \sqrt{\frac{U_e^* x^*}{\nu_e^*}}, \tag{4.5a,b}$$

respectively. Here, subscript e indicates the boundary layer edge values.

In order to solve the LST eigenvalue problem for a compressible boundary layer, the linear stability solver by Mack (1965, 1969, 1987) was employed. Mack's linear stability solver is based on the flat-plate equations and does not account for transverse curvature and body divergence. However, it accounts for the change in azimuthal wavelength with the streamwise location. For the linear stability analysis, self-similar compressible boundary layer profiles were used as base flow by employing Mangler transformation (Mangler 1948). Contours of constant amplification rate (stability diagram) for axisymmetric disturbances ($k_c = 0$) are presented in figure 7. The first- and second-mode unstable frequency bands are clearly distinguishable as they are separated by a stable region. The beginning and the end of the computational domain is also indicated in the stability diagram in figure 7.

Prior to conducting the fundamental breakdown simulations, DNS with very low amplitudes were performed such that the linear regime was maintained throughout the entire computational domain. These simulations allow a direct comparison of the DNS results with LST. In figure 8 the streamwise wavenumber α from the DNS
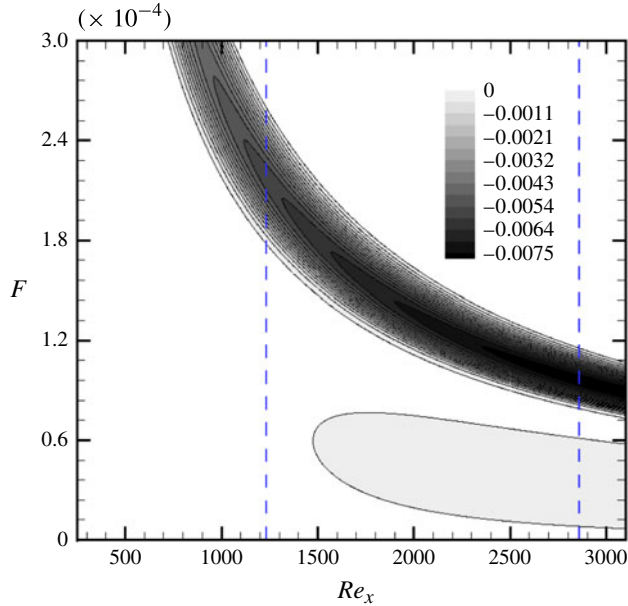
FIGURE 7. (Colour online) Contours of constant amplification rate α_i for axisymmetric disturbances ($k_c = 0$). Generated using Mack's LST solver (Mack 1965, 1987). The low-frequency band in the diagram corresponds to the first-mode unstable region and the high-frequency band represents the second-mode unstable region. The vertical dashed lines indicate the beginning and the end of the computational domain used in the DNS.

is compared with that from LST for axisymmetric disturbance waves with three different frequencies of $F = 1.1312 \times 10^{-4}$, $F = 1.1731 \times 10^{-4}$ and $F = 1.2318 \times 10^{-4}$. In the DNS the complete Navier–Stokes equations are employed and therefore the non-parallel effects are also included (Gaster 1974; Saric & Nayfeh 1975; Fasel & Konzelmann 1990). Hence, the spatial growth rate, α_i, depends on the criterion used. Here, the spatial growth rate and the streamwise wavenumbers were calculated based on the wall pressure disturbance as follows:

$$\alpha_i = -\frac{\mathrm{d}}{\mathrm{d}x}\left[\ln\left(A(x)|_{p'_{wall}}\right)\right], \quad \alpha_r = \frac{\mathrm{d}}{\mathrm{d}x}\left[\theta(x)|_{p'_{wall}}\right]. \quad (4.6a,b)$$

Here A represents the amplitude and θ the phase of the wall pressure disturbance. The streamwise distributions of amplitude $A(x)$ and phase $\theta(x)$ were obtained by performing Fourier transformations of the time signal of wall pressure disturbance. There is very good agreement between the growth rates and streamwise wavenumbers from DNS and LST (generally the streamwise wavenumber is less sensitive to the criterion used and therefore non-parallel effects are less obvious). Close to the disturbance forcing location, however, the streamwise wavenumber α_r and the spatial growth rate α_i as calculated from the DNS data, are modulated by the superposition of damped waves. This modulation is more pronounced for the spatial growth rate α_i than for the streamwise wavenumber α_r. Close to the location where the waves exhibit maximum growth rate there is good agreement between the spatial amplification rate α_i from DNS and LST. The reason for the small differences in spatial growth rate α_i at other locations is most likely due to non-parallel effects.
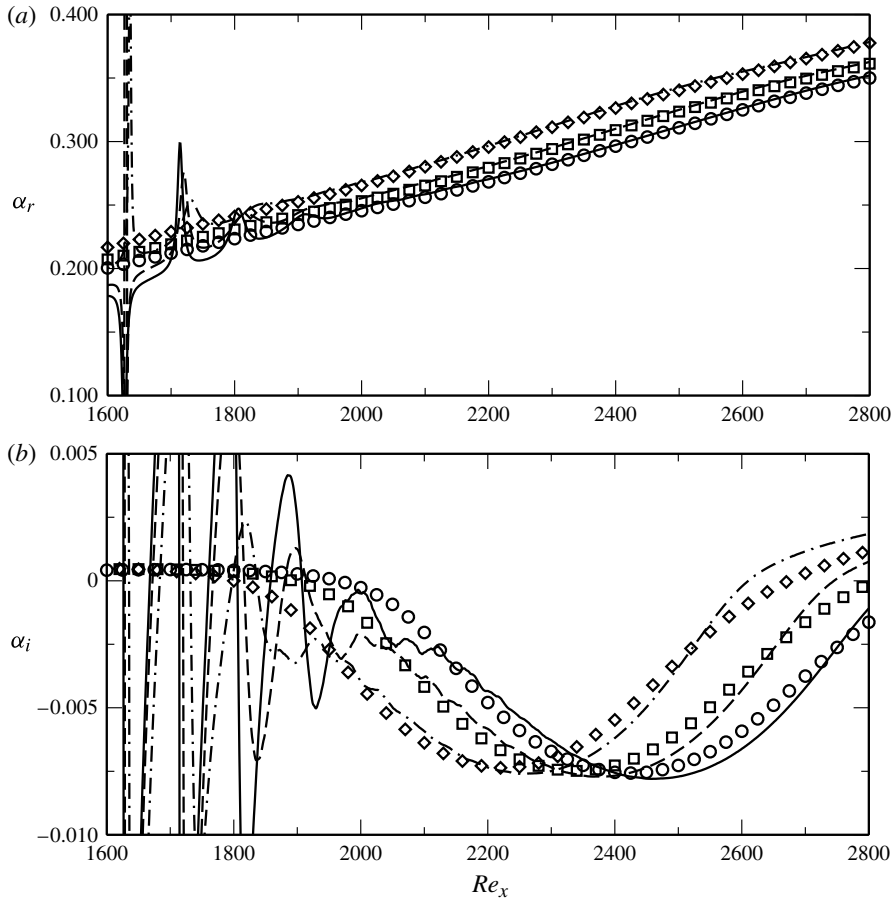
FIGURE 8. Downstream development of the complex streamwise wavenumber α obtained by LST (symbols) and DNS (using low-forcing amplitude) for axisymmetric waves ($k_c = 0$) with three different frequencies: $F = 1.1312 \times 10^{-4}$ (——, $\bigcirc$), $F = 1.1731 \times 10^{-4}$ (- - - -, $\square$) and $F = 1.2318 \times 10^{-4}$ (—·—·—, $\diamondsuit$). (*a*) α_r (streamwise wavenumber) and (*b*) α_i (spatial amplification rate). LST results were computed using Mack's solver (Mack 1965, 1987).

In figure 9 the wall-normal amplitude and phase distributions for the streamwise velocity component, temperature and pressure from the DNS are compared at $R_x = 2501$ to results obtained by LST using Mack's stability solver for axisymmetric disturbance waves with frequency $F = 1.1312 \times 10^{-4}$. The amplitude distributions from both linear theory and DNS are normalized by their respective maximum values. The excellent agreement between both results substantiates that the linear eigenbehaviour of the unstable mode is correctly reproduced in the DNS. The agreement with theory confirms that the disturbances introduced via the blowing and suction slot indeed initiate the desired physically relevant instability waves.

4.2. *Parameter study*

Fundamental resonance or (K- or Klebanoff-type) breakdown (Herbert 1988; Kachanov 1994) is due to a secondary instability mechanism involving a two-dimensional (here an axisymmetric) primary wave (1, 0) and a symmetric pair of oblique secondary
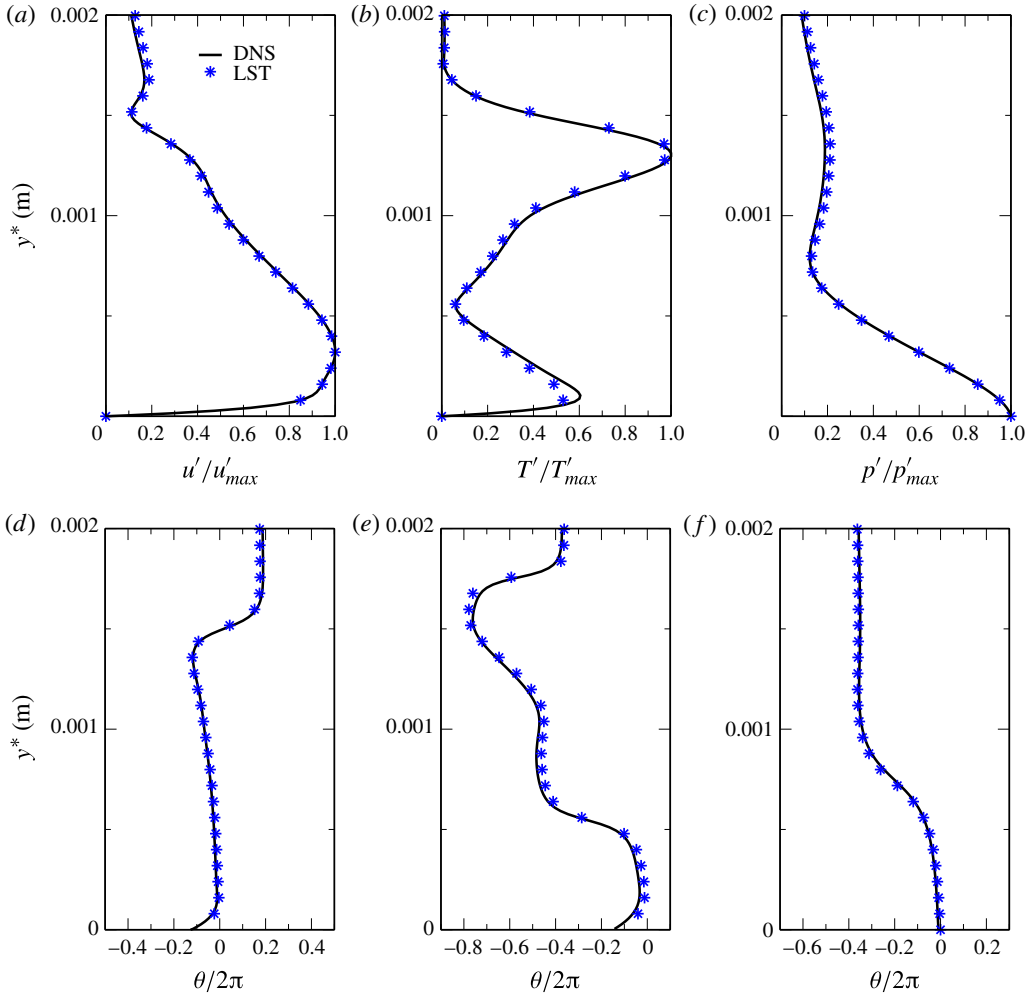
FIGURE 9. (Colour online) Comparison of wall-normal amplitude (*a–c*) and phase distribution (*d–f*) of the streamwise velocity, temperature and pressure disturbance to theoretical predictions from LST for frequency $F = 1.1312 \times 10^{-4}$ and azimuthal mode number $k_c = 0$ (axisymmetric disturbance wave) at $Re_x = 2501$. LST results were computed using Mack's solver (Mack 1965, 1987).

waves ((1, 1) and (1, −1)) of the same frequency. Note that in the present paper, a wave is denoted by (n, k), where *n* represents the frequency and *k* the azimuthal wavenumber, both normalized by the corresponding values of the secondary pair of oblique waves. For the incompressible case of fundamental resonance, for a flat plate, the strength of the fundamental resonance is strongly influenced by the amplitude of the primary wave $(1, 0)$ and the wave angle of the secondary oblique wave pair. For a cone this issue is even more complicated than for a flat plate, because the wave angle of a disturbance wave changes in the downstream direction. Therefore, we first performed a parameter study to find the most strongly resonating oblique wave pair. Then, we performed a set of highly resolved controlled fundamental breakdown simulations using the most strongly resonating oblique wave pair as secondary waves.
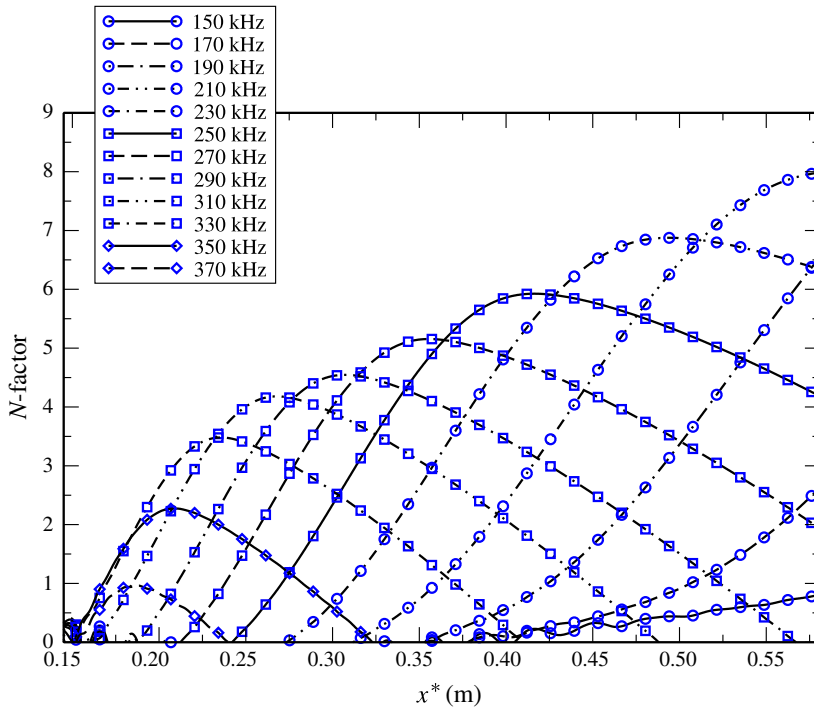
FIGURE 10. (Colour online) *N*-factor curves for axisymmetric waves ($k_c = 0$) obtained from a low-amplitude wavepacket simulation.

Fundamental resonance is initiated by forcing the primary wave $(1, 0)$ at a large amplitude and the secondary disturbance waves $(1, \pm 1)$ at a low amplitude. The dominant (linearly most amplified) axisymmetric wave was chosen as the primary wave, which was found from comparing the *N*-factors for axisymmetric waves for various frequencies. The streamwise development of the *N*-factors is plotted in figure 10 for axisymmetric disturbance waves ($k_c = 0$) as obtained from a low-amplitude wavepacket simulation (see for example Sivasubramanian & Fasel 2014). The *N*-factor of an instability wave is defined as

$$N_{n,k_c}(x) = \ln \left(\frac{A_{n,k_c}(x)}{A_{n,k_c,0}} \right), \qquad (4.7)$$

where the subscript n and k_c denote the frequency and azimuthal wavenumber of the wave, respectively; $A_{n,k_c}(x)$ is the amplitude of the disturbance wave at a certain downstream position and $A_{n,k_c,0}$ is the amplitude of the disturbance wave at its lower neutral point. The amplitudes of the disturbance waves were obtained by performing Fourier transformations of the time signal of the disturbance waves. In figure 10 the *N*-factor reached by the most amplified axisymmetric wave ($k_c = 0$) is approximately 8.0 with a corresponding non-dimensional frequency of $F = 1.1312 \times 10^{-4}$ ($f^* \approx$ 210 kHz). It was therefore chosen as the primary wave $(1, 0)$ for a parameter study to determine the most strongly resonating oblique secondary wave pair $(1, \pm 1)$.

Towards this end a series of low-resolution simulations was performed for various azimuthal wavenumbers (k_c). The results from this parameter study are presented in
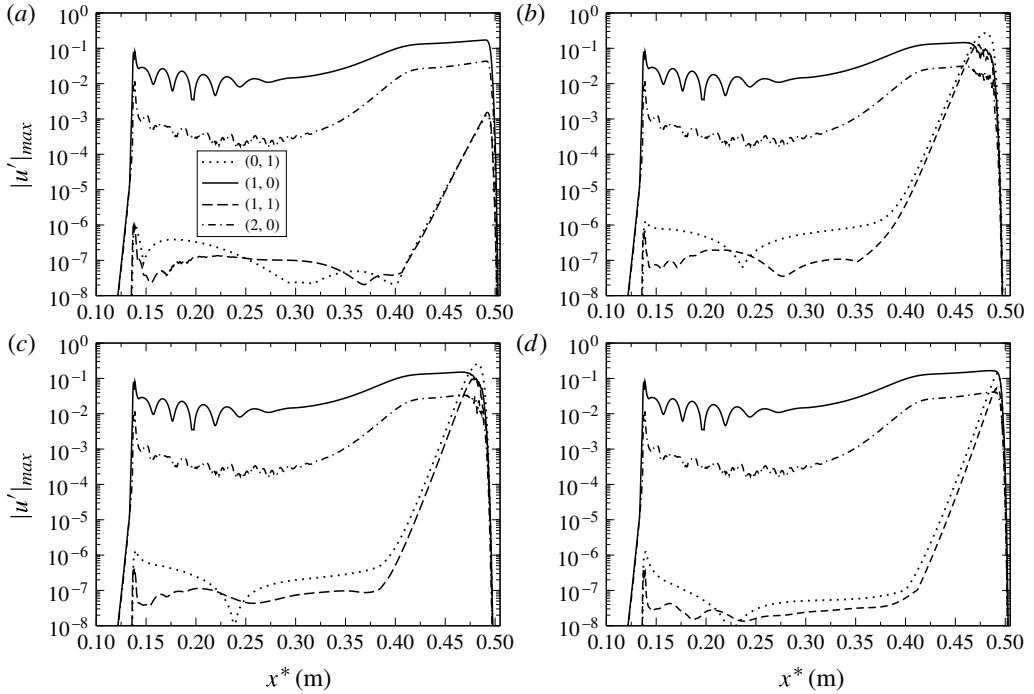
FIGURE 11. Maximum of streamwise velocity disturbance versus downstream distance for the cases with azimuthal wavenumber (*a*) $k_c = 60$, (*b*) $k_c = 80$, (*c*) $k_c = 100$ and (*d*) $k_c = 120$. Shown are selected modes, which play an important role in the early nonlinear stage of fundamental resonance.

figures 11 and 12. In figure 11, the downstream amplitude development of selected modes is shown for the low-resolution simulation performed for azimuthal mode numbers $k_c = 60$, 80, 100 and 120. These curves were obtained from the wall-normal maximum of the streamwise velocity disturbances. As can be observed in figure 11, when the axisymmetric primary wave $(1, 0)$ exceeds a certain amplitude, the secondary oblique wave pair $(1, \pm 1)$ and the steady longitudinal vortex mode $(0, 1)$ experience strong secondary growth. Figure 12 shows the growth rate (σ) of the secondary oblique wave pair $(1, \pm 1)$ as a function of azimuthal mode number (k_c). The growth rates (σ) were extracted at the streamwise position $x^* = 0.46$ m ($R_x = 2501$). A broad band of azimuthal modes experiences resonant secondary growth, but according to figure 12, waves with $k_c = 100$ exhibit the strongest secondary growth rate.

4.3. *High-resolution fundamental breakdown simulations*

In the parameter study discussed above for fundamental resonance, oblique waves with azimuthal mode number $k_c = 100$ were identified as the most strongly resonating oblique waves. Therefore, a highly resolved fundamental breakdown simulation (CFUND1) was performed with azimuthal mode $k_c = 100$ for the secondary wave pair. In these simulations, the axisymmetric primary wave $(1, 0)$ with a frequency of $f^* \approx 210$ kHz was forced with a large amplitude ($A_{1,0} = 4.0\%$ of the free-stream velocity) and the oblique secondary waves $(1, \pm 1)$ were forced at a low amplitude ($A_{1,\pm 1} = 0.1\%$ of the free-stream velocity). Here each of the two modes $(1, 1)$ and $(1, -1)$ are forced with the same amplitude of 0.1% of the free-stream velocity.
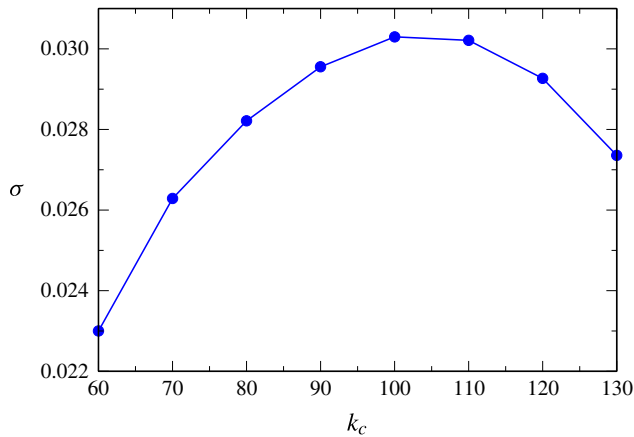
FIGURE 12. (Colour online) Fundamental secondary growth rate (σ) as a function of azimuthal mode number (k_c).

The downstream development of the wall-normal amplitude maximum of the streamwise velocity disturbance is presented in figure 13. Selected modes that play an important role in the nonlinear stages of the fundamental breakdown are shown. As before, when the axisymmetric primary wave $(1, 0)$ reaches a certain amplitude (at $x^* \sim 0.4$ m), resonance sets in and the secondary mode $(1, 1)$ and the steady longitudinal vortex mode $(0, 1)$ start to grow much faster than the primary wave and eventually reach the same amplitude levels as the primary mode $(1, 0)$ at $x^* \sim 0.45$ m. As the steady longitudinal vortex mode $(0, 1)$ starts to grow, it also produces mean flow distortion (mode $0, 0$). Higher harmonic modes $(2, 0)$, $(2, 1)$ and $(1, 2)$ are also generated. When the amplitudes of modes $(1, 1)$ and $(0, 1)$ approach the amplitude of the primary mode $(1, 0)$ all higher modes experience rapid streamwise growth and the transition process becomes strongly nonlinear, which is an indication of the onset of the final breakdown to turbulence. As more and more higher steady modes $((0, 2), (0, 3), (0, 4), (0, 5)$ etc.) are generated, the mean flow deformation (mode $0, 0$) increases. Note that in the nonlinear region, the steady longitudinal vortex mode $(0, 1)$ has the highest amplitude (0.45 m $< x^* < 0.57$ m). Close to the end of the computational domain the steady longitudinal vortex mode $(0, 2)$ reaches higher amplitudes than $(0, 1)$. However, the steady mode $(0, 0)$ has the highest amplitude, indicating a strong mean flow distortion due to transition to turbulence. A more detailed presentation of the downstream development of the wall-normal amplitude maximum of the streamwise velocity disturbance is provided in figure 14. Modes with the fundamental frequency $(1, k)$, two-dimensional modes $(h, 0)$ and three-dimensional modes $(h, 1)$ are presented in figures 14(a), 14(b) and 14(c), respectively. They provide a detailed view of how the spectrum broadens due to nonlinear interactions, which produce higher modes as the flow transitions from the laminar to the turbulent state.

The downstream development of the temporally and azimuthally averaged skin friction coefficient, C_f, is shown in figure 15(a). The skin friction coefficient is calculated as

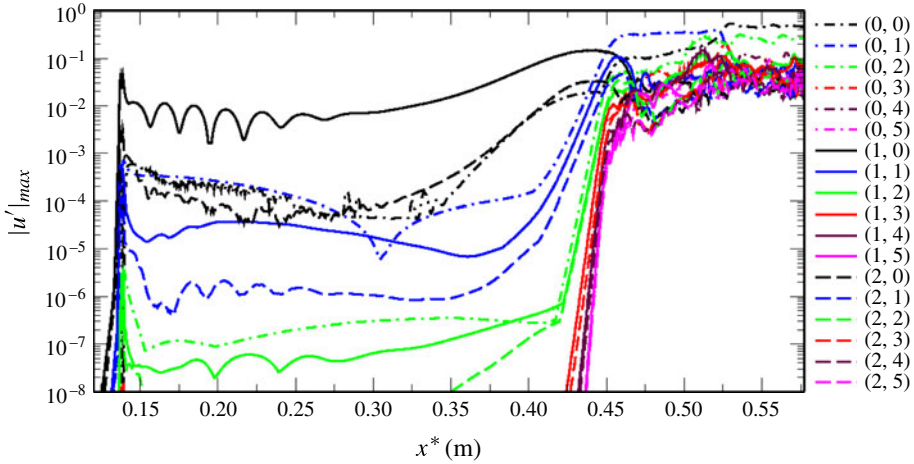$$c_f = \frac{2\overline{\mu} \left.\dfrac{\partial \overline{u}}{\partial y}\right|_{y=0}}{Re}. \tag{4.8}$$

FIGURE 13. (Colour online) Streamwise development of the maximum *u*-velocity disturbance amplitude obtained from the fundamental breakdown simulation. Note that when the axisymmetric primary wave $(1, 0)$ reaches a certain amplitude, the secondary mode $(1, 1)$ and the steady longitudinal vortex mode $(0, 1)$ grow faster than the primary wave and eventually reach the same amplitude as the primary mode. Higher harmonics, modes $(2, 0)$ and $(2, 1)$, are also generated, and when modes $(1, 1)$ and $(0, 1)$ approach the amplitude of the primary mode $(1, 0)$ all higher modes experience rapid streamwise growth. In the nonlinear region the steady longitudinal vortex mode $(0, 1)$ has the highest amplitude. Close to the end of the computational domain, however, the steady mode $(0, 2)$ reaches higher amplitudes than $(0, 1)$.

The Reynolds number, Re, is based on the reference length, L^*, and the flow quantities in the free stream. Note that symbols with an overbar, $\bar{\phi}$, represent Reynolds-averaged, i.e. time- and spanwise-averaged, flow quantities. The skin friction curves obtained from the simulations were compared with a correlation for a turbulent boundary layer from White (2006),

$$c_{f,plate} \sim \frac{0.455}{\left(S \ln\left[\dfrac{0.06}{S} Re_{xe} \dfrac{\mu_e}{\mu_w} \sqrt{\dfrac{T_e}{\overline{\overline{T}}_w}}\right]\right)^2}. \tag{4.9}$$

Here, the subscript *e* refers to boundary layer edge conditions and the subscript *w* refers to wall conditions. The factor *S* can be obtained from

$$S = \frac{\left(\dfrac{\overline{T}_{aw}}{T_e} - 1\right)^{1/2}}{\arcsin(A) + \arcsin(B)}, \tag{4.10}$$

with *A* and *B* defined as

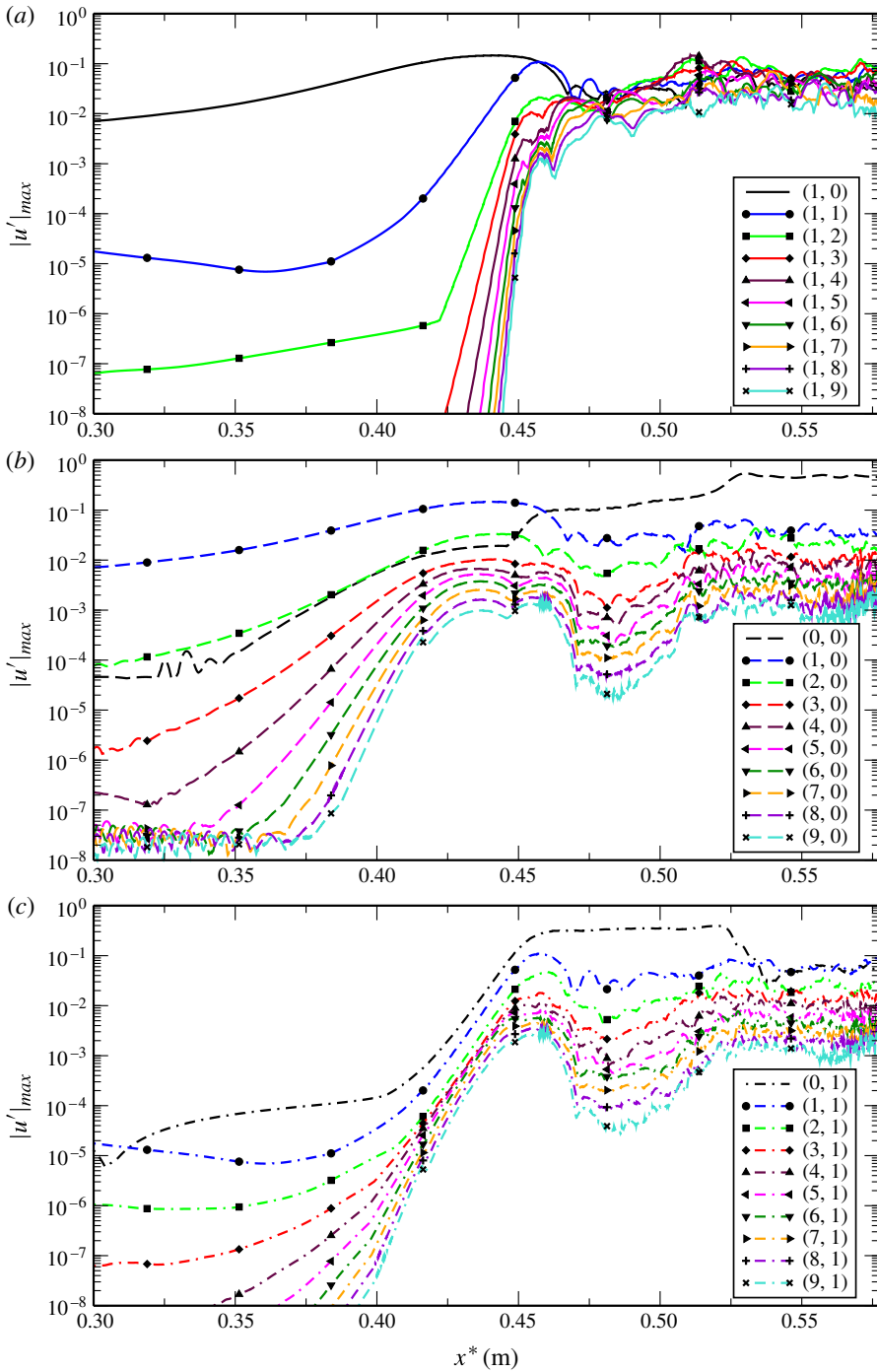$$A = \frac{2a^2 - b}{\sqrt{b^2 + 4a^2}} \quad \text{and} \quad B = \frac{b}{\sqrt{b^2 + 4a^2}}, \tag{4.11a,b}$$

FIGURE 14. (Colour online) Detailed presentation of the streamwise development of the maximum *u*-velocity disturbance amplitude obtained from the fundamental breakdown simulation. (*a*) Modes with fundamental frequency $(1, k)$; (*b*) two-dimensional modes $(h, 0)$ and (*c*) three-dimensional modes $(h, 1)$.
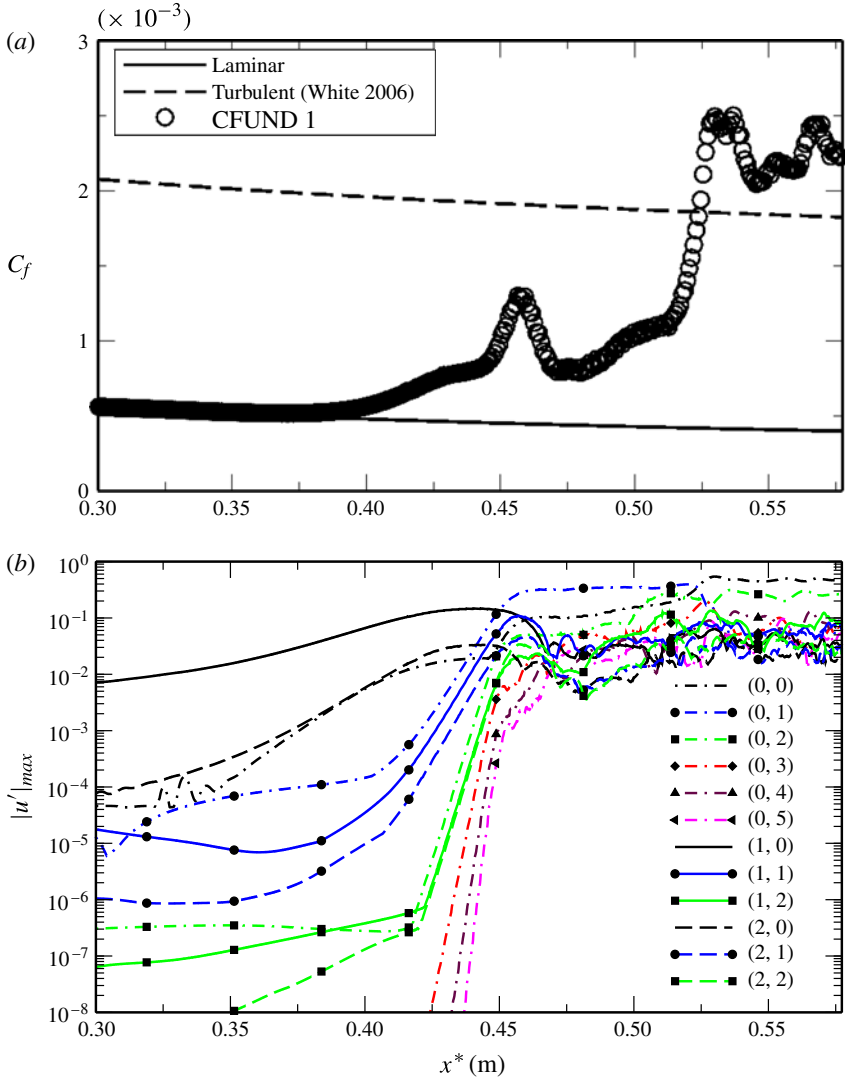
FIGURE 15. (Colour online) (*a*) Time- and azimuthal-averaged skin friction coefficient and (*b*) streamwise development of the maximum *u*-velocity disturbance amplitude for the fundamental breakdown simulation. The initial rise in skin friction is caused by the large-amplitude primary wave $(1, 0)$. This is followed by a dip caused by the nonlinear saturation of the primary wave $(1, 0)$. Then a steeper rise in skin friction occurs when all higher modes experience nonlinear growth.

where *a* and *b* are given by

$$a = \sqrt{\frac{\gamma - 1}{2} M_e^2 \frac{T_e}{\overline{T}_w}} \quad \text{and} \quad b = \left(\frac{\overline{T}_{aw}}{\overline{T}_w} - 1 \right), \qquad (4.12a,b)$$

respectively. Note that $\overline{T}_{aw}$ denotes the adiabatic wall temperature for a turbulent boundary layer at the same flow conditions. Since this value is not known, it has to

be estimated using the turbulent recovery factor (White 2006; Roy & Blottner 2006),

$$r_{turb} \sim (Pr)^{1/3} \sim 0.9. \tag{4.13}$$

The above relationship used for estimating the skin friction is only valid for a turbulent flat-plate boundary layer. Therefore, a correction for the cone geometry was employed as suggested by van Driest (1952) and White (2006) based on the von Kármán momentum integral: $C_{f,cone} = G \times C_{f,plate}$, where $1.1 < G < 1.15$. Note that the theoretical turbulent skin friction curve in figure 15(a) is calculated with $G = 1.1$. The skin friction plotted in figure 15(a) initially follows the laminar curve up to $x^* \sim 0.38$ m, then it increases from the laminar curve towards the turbulent curve. However, farther downstream it unexpectedly drops sharply to almost the laminar value before rising again steeply and eventually overshooting the turbulent skin friction curve. The skin friction curve suggests that the boundary layer is close to a turbulent boundary layer at the end of the computational domain.

A close examination of the results shown in figure 15(a,b) reveals that the initial deviation of the skin friction from its laminar value is due to the large amplitude reached by the primary wave (1, 0). The first peak in the skin friction corresponds to the streamwise location where the primary wave (1, 0) seems to 'saturate' ($x^* \sim 0.45$ m). This peak in skin friction also roughly coincides with the location where the secondary disturbances (e.g. modes (1, $\pm$1) and (0, 1)) reach their largest amplitude levels, which in turn cause a mean flow deformation (0, 0). Due to the mean flow deformation the primary wave starts to decay following its 'nonlinear saturation' and the skin friction dips almost to the laminar value. Together with the primary wave, higher modes also starts to decay (seen clearly in figure 14b,c at $x^* \sim 0.46$ m). Following the dip, a much steeper rise in the skin friction occurs as all higher modes experience very strong nonlinear amplification ($x^* \sim 0.52$ m). As a result of this steep rise, the skin friction overshoots the theoretical turbulent skin friction estimate.

Note that this particular development of the skin friction is probably due to the 'controlled' transition scenario where only a few selected waves are forced initially. In a 'natural' transition scenario this development may be less pronounced or even completely absent. Also note that the mode (0, 0) is the only mode that directly affects the development of the temporally and azimuthally averaged skin friction coefficient. All other modes influence the skin friction development indirectly through their nonlinear effect on the development of mode (0, 0). More importantly, the maximum amplitude of mode (0, 0) does not seem to decay noticeably here. Therefore, it is the change in the shape of mode (0, 0) that influences the skin friction development and causes the dip following the first peak. Hence, the change in the shape of mode (0, 0) may very well be connected to the decay of the primary mode (1, 0) and other higher modes after the first peak in skin friction. These results raise the interesting question of whether the first peak in the skin friction could be influenced by the amplitude of the oblique secondary wave pair (1, $\pm$1).

In order to answer this question, we performed two more 'controlled' fundamental breakdown simulations, CFUND 2 and CFUND 3, where the forcing amplitudes for the oblique secondary waves were changed to 0.01 % and 1.0 % of the freestream velocity, respectively. The forcing amplitude for the primary wave was kept the same as in CFUND 1 (4.0 % of the free-stream velocity). A summary of the forcing parameters used in these fundamental breakdown simulations is provided in table 3. For selected modes, the streamwise velocity disturbances development from CFUND 2 and CFUND 3 are plotted in figure 16. Overall, the downstream

	CFUND 1	CFUND 2	CFUND 3
$A_{[1,0]}$	0.04	0.04	0.04
$A_{[1,\pm1]}$	1.0×10^{-3}	1.0×10^{-4}	1.0×10^{-2}

TABLE 3. Forcing parameters for the fundamental breakdown simulations. Note that the notation $[n, k]$ is used in order to identify a particular wave according to its frequency n and its azimuthal wavenumber k; n denotes multiples of the fundamental forcing frequency $f^* = 210$ kHz and k multiples of the azimuthal wavenumber.

amplitude development looks very similar to CFUND 1. However, the time- and azimuthally averaged skin friction coefficients from CFUND 2 and CFUND 3 as plotted in figure 18 look slightly different. As the forcing amplitude of the oblique secondary waves is decreased (CFUND 2) the first peak in the skin friction distribution shifts slightly downstream. This is due to the fact that the secondary growth of the oblique wave starts at a lower amplitude level and therefore reaches nonlinear amplitudes slightly downstream. However, when the forcing amplitude of the oblique secondary waves is increased (CFUND 3), the first peak shifts slightly upstream. Here, it is due to the fact that the secondary growth of the oblique wave starts at a higher amplitude level and consequently reaches nonlinear amplitudes slightly upstream. As a result, the onset of the rapid streamwise growth of higher modes also shifts slightly downstream in CFUND 2 and shifts slightly upstream in CFUND 3 with increasing forcing amplitude of secondary waves (see figure 16*a*,*b*). In CFUND 2 and CFUND 3, as the primary wave is forced with the same amplitude as in CFUND 1, the location of transition onset remains the same for all three cases. This confirms that the initial rise in skin friction (onset of transition) is due to the large amplitude of the primary wave (1, 0). A comparison of the streamwise development of the key modes between CFUND 1, CFUND 2 and CFUND 3 is provided in figure 17. Figure 17(*a*) clearly presents that the secondary wave (1, 1) reaches nonlinear amplitudes downstream and upstream (compared to CFUND 1) in CFUND 2 and CFUND 3, respectively. Similarly, the steady mode (0, 1) reaches nonlinear amplitudes downstream and upstream compared to CFUND 1 and, as a consequence, induces mean flow deformation either downstream or upstream (see figure 17*b*).

The downstream development of the time- and azimuthal-averaged Stanton number, *St*, is presented in figure 19. The Stanton number distribution follows the laminar curve up to $x^* \sim 0.38$ m and then increases towards the turbulent curve. Eventually it overshoots the turbulent curve before dropping almost down to the laminar value. However, downstream it steeply increases again towards the turbulent curve and stays above the turbulent value curve. The stronger overshoots observed here, even in the transitional stages, at the streamwise location where the first peak appears for skin friction coefficient is unique and is a direct result of stronger temperature gradients produced by the transition process. Such overshoots during the transitional stages as observed here could lead to localized regions of very large heat transfer. The downstream development of the time-averaged skin friction and Stanton number along the streak is plotted in figure 20. The skin friction and Stanton number along the streak have much larger values compared to their azimuthal-averaged values and exhibit massive overshoots over the turbulent values both in the early and late transition region. Note that the particular development of the Stanton number
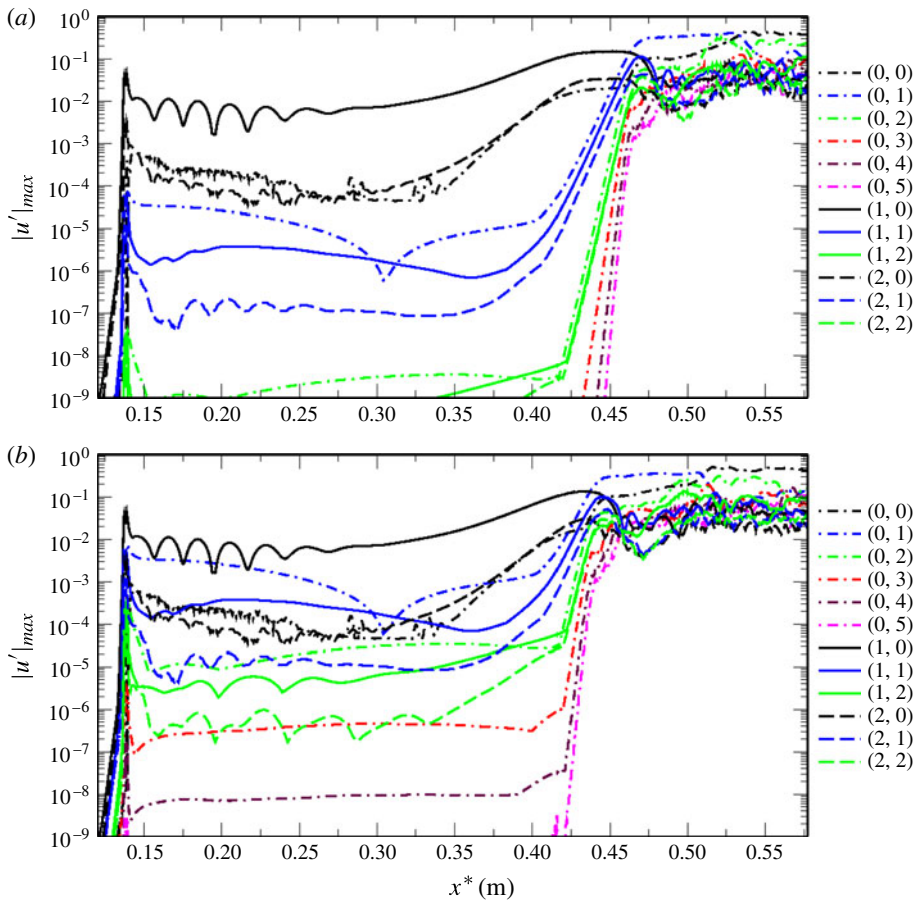
FIGURE 16. (Colour online) Streamwise development of the maximum u-velocity disturbance amplitude from CFUND 2 (a) and CFUND 3 (b). Shown are selected modes that play an important role in the early nonlinear stage of fundamental resonance.

observed here is strongly affected by the isothermal wall boundary condition used in the simulations presented in this paper.

Isocontours of the time-averaged skin friction and wall-normal temperature gradient (dT/dy) at the wall are shown in figures 21(a) and 21(b). Remarkable are the streamwise aligned 'hot' streaks, which are a consequence of the large amplitudes reached by the steady longitudinal vortex modes. The steady mode (0, 1) is the first to reach the highest amplitude and it is, therefore, responsible for the first upstream appearing streaks. Downstream, however, these streaks get weaker. As the steady mode (0, 2) reaches the highest amplitude close to the end of the computational domain, there, the azimuthal spacing of the streaks is related to that mode. These streaks look qualitatively similar to the streamwise pattern observed in the Purdue experiments (under quiet-flow conditions) for a flared cone using temperature-sensitive paint (see figure 7b in Berridge *et al.* 2010 and figure 18 in Ward *et al.* 2012). The associated streamwise temperature distribution obtained using temperature-sensitive-paint data first increases from the laminar reference value, then decreases downstream of the
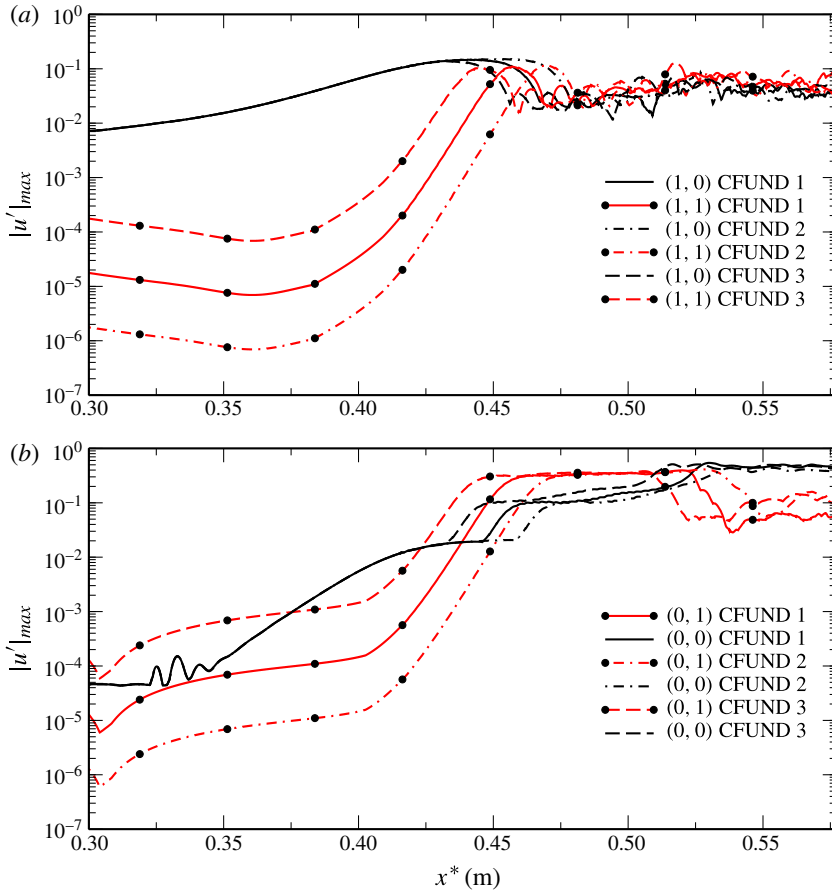
FIGURE 17. (Colour online) Comparison of the streamwise development of the maximum u-velocity disturbance amplitude of key modes from CFUND 1, CFUND 2 and CFUND 3.

first peak and finally increases again as the flow transitions to turbulence (see figure 11*a* in Berridge *et al.* 2010).

This behaviour is similar to the trend observed in heat transfer distributions obtained from the second-mode fundamental breakdown simulations (see figure 19). Under noisy-flow conditions, however, the streamwise streaks were not observed in the Purdue experiments (the Purdue tunnel can be run either as a quiet-flow tunnel or as a conventional noisy-flow tunnel). The streamwise temperature distribution measured under noisy-flow conditions (see figure 11*b* in Berridge *et al.* 2010) was also different from the distribution measured under quiet-flow conditions: it increased gradually from the laminar value to the turbulent value (as in Horvath *et al.* 2002). It is not understood why the streaks appear under quiet-flow and not under noisy-flow. Thus, the streamwise streaks and the streamwise temperature distribution measured in the Purdue experiments under quiet-flow conditions are similar to the streaks and the heat transfer curves obtained from the second-mode fundamental (K-type) breakdown simulations. Therefore, we conjecture that second-mode fundamental breakdown mechanism may have played a role in the natural transition process in the Purdue experiments under quiet-flow conditions. Overall, the simulations presented in this
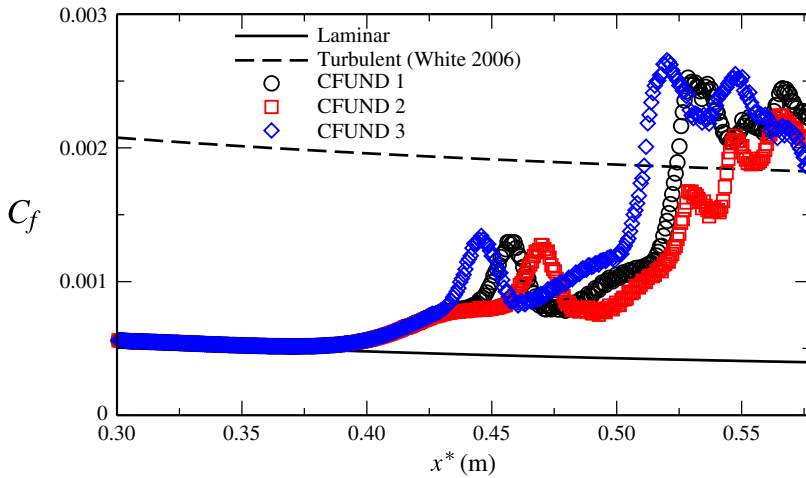
FIGURE 18. (Colour online) Time- and azimuthal-averaged skin friction coefficient from CFUND 1, CFUND 2 and CFUND 3.
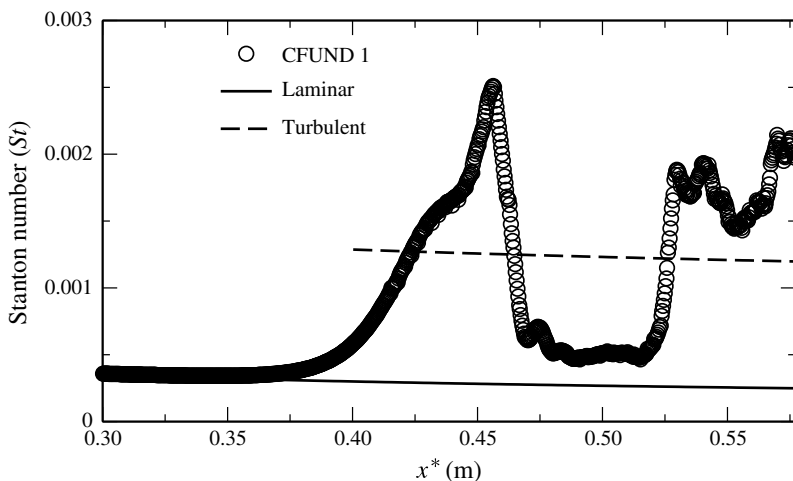

FIGURE 19. Time- and azimuthal-averaged Stanton number obtained from CFUND 1.

paper demonstrate that second-mode fundamental breakdown is a viable route to turbulence in hypersonic cone boundary layers at Mach 6 and confirms the findings of our previous research in which we investigated the 'natural' transition process in hypersonic cone boundary layers using wavepackets and identified second-mode fundamental breakdown to be a relevant mechanism for transition to turbulence in Mach 6 cone boundary layers.

4.4. *Flow structures*

A close observation of the dominant flow structures and their streamwise development can provide further insight into the underlying physical mechanisms of the transition process. In figure 22(*a*) the flow structures from the fundamental breakdown simulation are plotted using the Q criterion (Hunt, Wray & Moin 1988). The flow
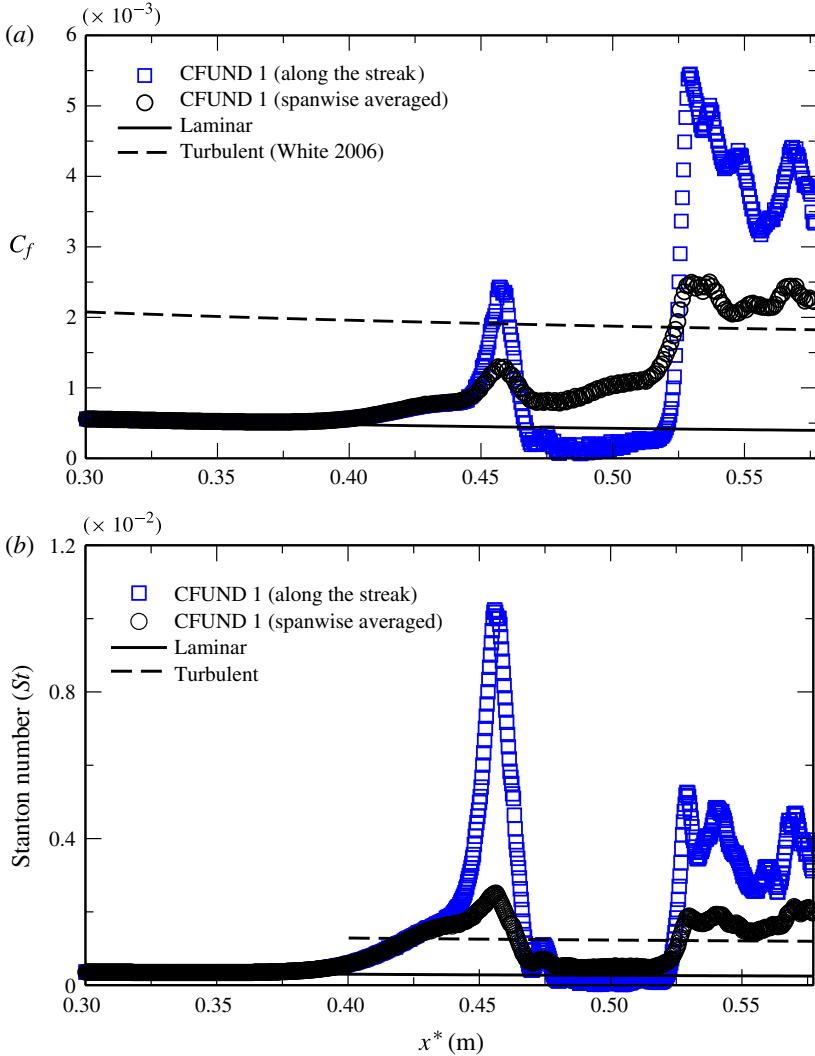
FIGURE 20. (Colour online) Time- and azimuthal-averaged (*a*) skin friction and (*b*) Stanton number obtained from CFUND 1.

structures reveal the typical evolution of a K-type breakdown: during the initial stage of the transition process the dominant wave is axisymmetric. Once nonlinear interactions cause the oblique secondary waves to amplify rapidly, the dominant axisymmetric waves become modulated (peak–valley splitting) in the circumferential direction (see figures 22*b* and 23*a*). Eventually, the interaction of the dominant axisymmetric wave and finite-amplitude oblique waves leads to the formation of Λ-vortices. The Λ-vortices appear in an aligned pattern because the primary axisymmetric wave and the secondary oblique waves have the same frequency. The evolution of the flow structures during the final stage of transition can be better observed in the close-up view of figures 23 and 24. The aligned arrangement of the Λ-vortices can be seen clearly. The tips of the Λ-vortices lift away from the surface while the legs remain close to the wall. Hairpin-shaped vortices start to appear on
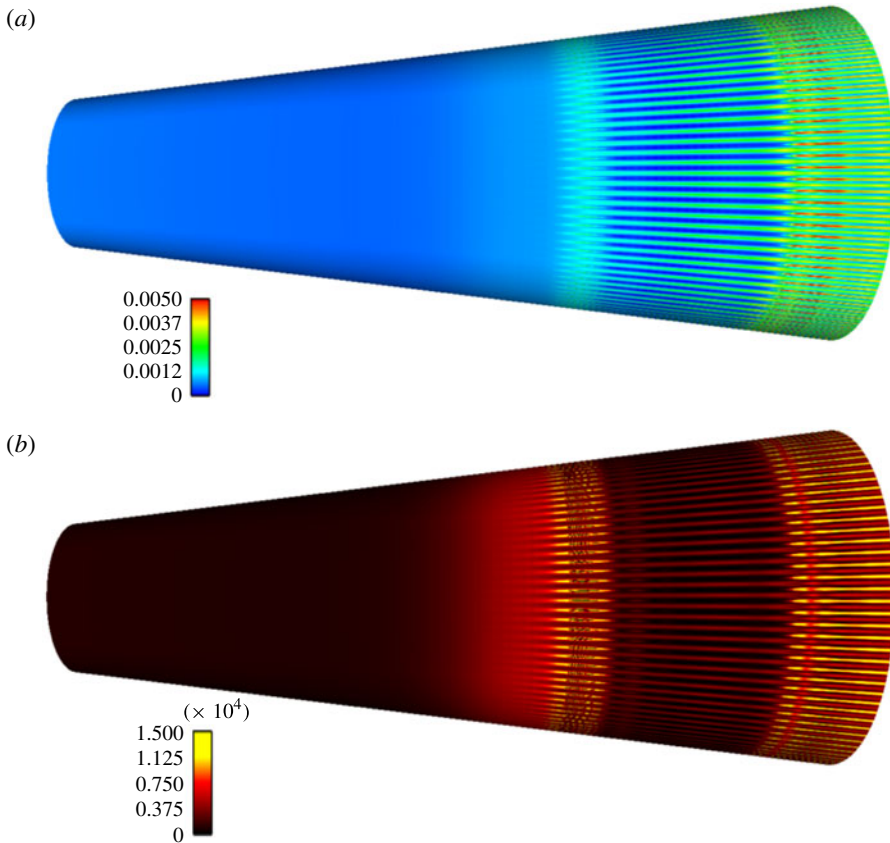
(*a*)

0.0050
0.0037
0.0025
0.0012
0

(*b*)

$(\times 10^4)$
1.500
1.125
0.750
0.375
0

FIGURE 21. (Colour online) Time-averaged (*a*) skin friction and (*b*) wall-normal temperature gradient ($\mathrm{d}T/\mathrm{d}y$) at the wall obtained from the fundamental breakdown simulation CFUND 1. The streamwise aligned 'hot' streaks look qualitatively similar to the streamwise streaks observed in the Purdue experiments using temperature-sensitive paint for a flared cone.

the tips of the Λ-vortices. Eventually these structures break down to smaller scales as the flow starts to become turbulent.

Instantaneous streamwise velocity contours are presented in the x–φ plane for three wall-normal positions inside the boundary layer (see figure 25). This figure illustrates various flow features such as the transition onset, the breakup region and the early turbulent region close to the wall (figure 25*a*) and farther away (figure 25*c*). Dark regions denote low-velocity flow and brighter regions correspond to high-velocity flow. Two-dimensional structures seem to appear upstream in figure 25 for all three wall-normal positions. These structures correspond to the second-mode axisymmetric wave (primary wave) forced at a high amplitude. Farther downstream these two-dimensional structures appear modulated in the azimuthal direction due to nonlinear interactions between the axisymmetric primary wave and the secondary oblique waves. The azimuthal modulation becomes stronger downstream, indicating the presence of strong oblique waves (generated by nonlinear interactions). Furthermore, the aligned arrangements characteristic of K-type transition are clearly
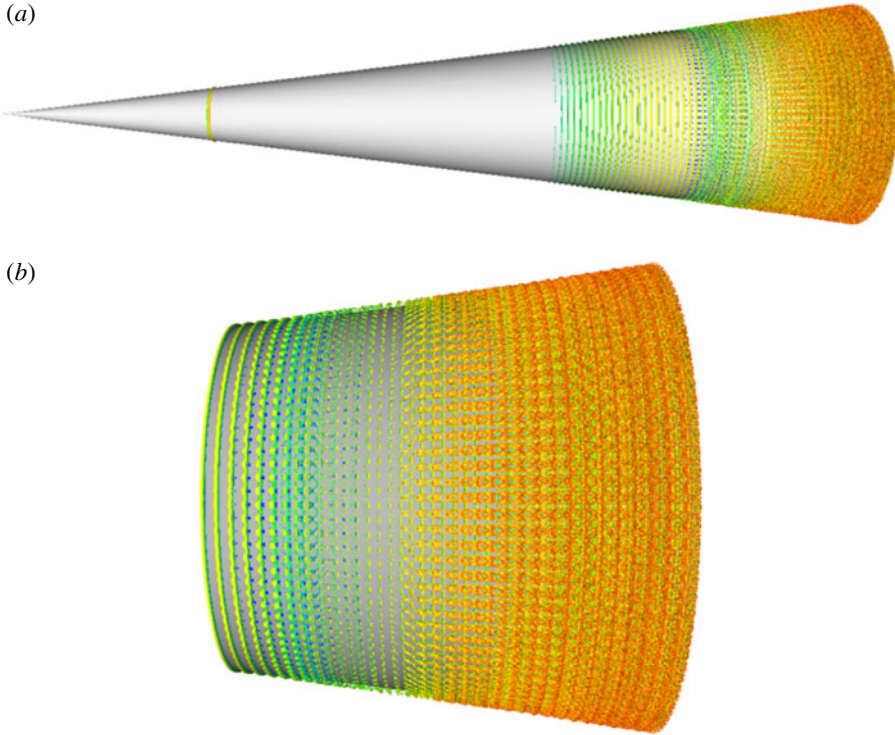
(*a*)

(*b*)

FIGURE 22. (Colour online) Visualization of flow structures using isosurface of Q criterion ($Q = 20\,000$) obtained from the fundamental breakdown simulation CFUND 1. (*a*) Full view of the cone and (*b*) last downstream part of the cone. The isosurfaces are coloured by the streamwise velocity magnitude.

visible (see for example figure 25*b*). Eventually the flow breaks up into small-scale structures as the flow transitions to turbulence.

   To gain more information about the dynamics of the flow field during the transition process, contours of the instantaneous spanwise vorticity component are plotted in the x–y plane for various azimuthal positions (see figure 26). The five selected azimuthal positions are (*a*) $\varphi = 0$ (0°), (*b*) $\varphi = 0.0078$ (0.45°), (*c*) $\varphi = 0.0157$ (0.9°), (*d*) $\varphi = 0.0235$ (1.35°) and (*e*) $\varphi = 0.0314$ (1.8°). Here dark contour regions represent negative spanwise vorticity and white regions represent positive spanwise vorticity. Figure 26 provides a detailed view of the breakdown region and the downstream development of the small-scale structures. The plane at $\varphi = 0$ is located in the spanwise valley location and the plane at $\varphi = 0.0314$ is in the spanwise peak location. In the plane at $\varphi = 0.0314$ (spanwise peak), prior to breakdown (up to $x^* \sim 0.51$ m) a strong concentration of spanwise vorticity can be observed away from the wall. Downstream of this location ($x^* \sim 0.51$ m), for all azimuthal positions, the flow is dominated by small-scale structures.

   Contours of the instantaneous wall-normal density gradient are shown in figure 27 for several azimuthal positions. The selected azimuthal positions are the same as in figure 26. As before, wall-normal density gradient contours are shown in the x–y plane for each azimuthal position. This type of flow visualization could be used for comparison with schlieren photographs which would reveal flow structures in
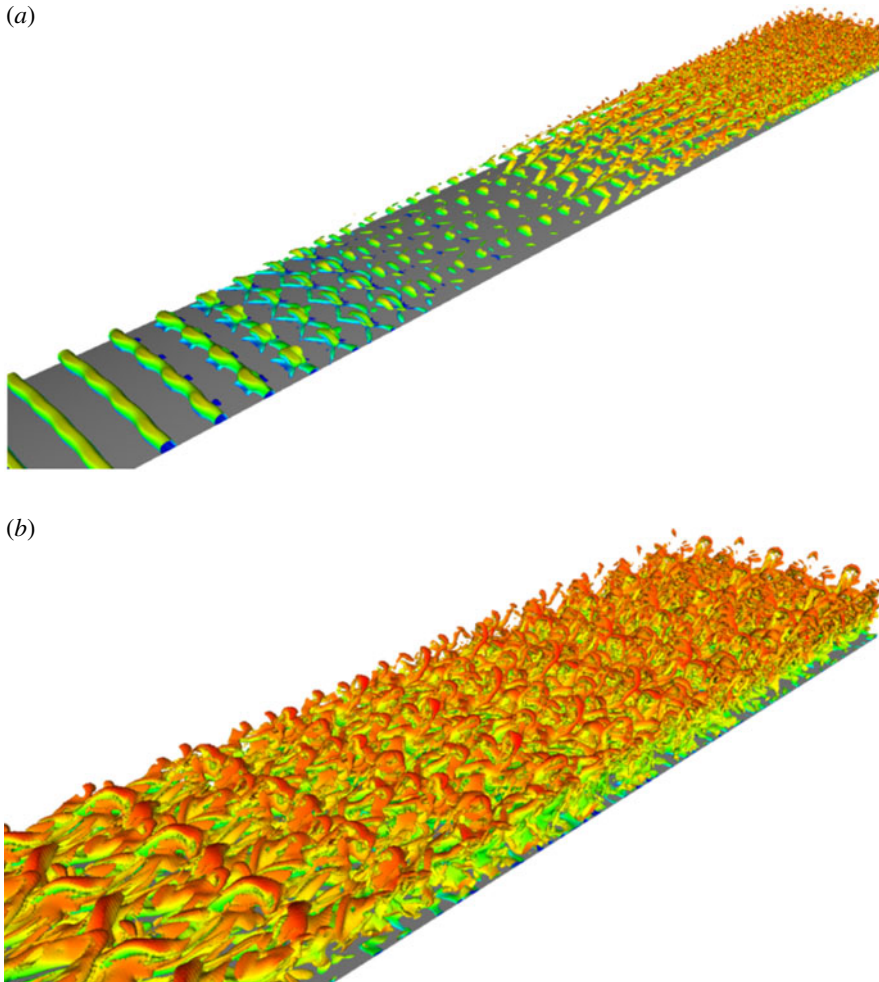
(*a*)

(*b*)

FIGURE 23. (Colour online) Visualization of flow structures using isosurface of Q criterion ($Q = 20\,000$) obtained from the fundamental breakdown simulation CFUND 1: (*a*) close-up view of a small section of the cone; (*b*) close-up view of the last downstream part. The isosurfaces are coloured by the streamwise velocity magnitude.

high-speed experiments. At all azimuthal positions 'rope-like' structures appear close to the boundary layer edge up to the location where the flow starts to break down. Such structures have been observed in hypersonic boundary layer flows by several experimentalists (see for example Lachowicz *et al.* 1996). Flow visualization from the numerical simulations by Pruett & Chang (1995) and Pruett & Chang (1998) also clearly reveals instability waves of rope-like appearance. The structures observed in our simulation are qualitatively similar in appearance to the schlieren image obtained by Lachowicz *et al.* (1996) and to the flow visualization by Pruett & Chang (1998). The wavelength of these structures is approximately twice the boundary layer thickness, which is consistent with the nature of the second-mode instability waves. Furthermore, as the boundary layer starts to break down, acoustic waves 'radiating' away from the boundary layer and towards the free stream are also observed for all azimuthal positions (see figure 27).
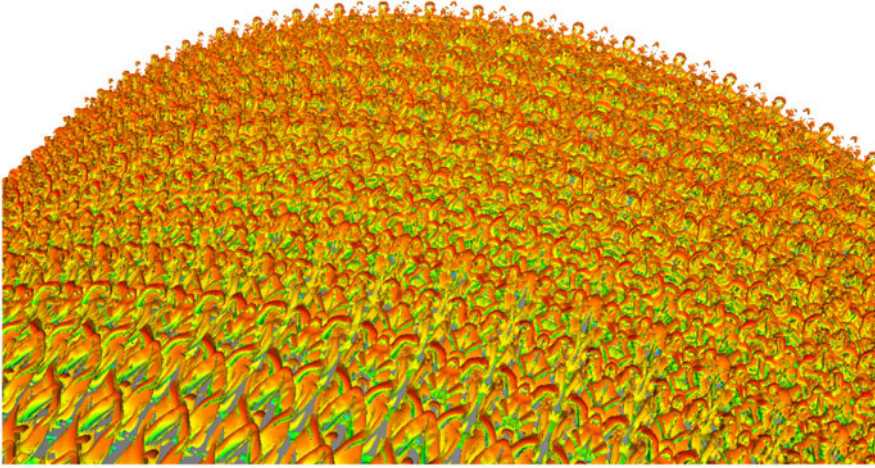
FIGURE 24. (Colour online) Visualization of flow structures using isosurface of Q criterion ($Q = 20\,000$) obtained from the fundamental breakdown simulation CFUND 1. Close-up view of the last downstream part of the cone. The isosurfaces are coloured by the streamwise velocity magnitude.

4.5. *Quantitative analysis*

For quantitative global analyses, the time- and azimuthal-averaged streamwise velocity and temperature profiles shown in figures 28 and 29 are inspected. The time interval over which the relevant data were extracted and averaged is equal to four forcing periods of the primary wave. Figure 28(*a,b*) shows isocontours of streamwise velocity and temperature in the *x*–*y* plane, whereas figure 29(*a,b*) shows wall-normal profiles extracted at different downstream positions (rescaled with the local boundary layer thickness). The objective here is to show how these profiles develop during transition and how they converge to a turbulent profile. It is clear from these plots that with increasing downstream distance, the boundary layer thickness is increasing and the mean streamwise velocity and temperature profiles are becoming 'fuller', which is a consequence of the transition to turbulence.

The downstream development of the shape factor,

$$H_{12} = \frac{\delta^*}{\theta}, \qquad (4.14)$$

and the Reynolds number based on the momentum thickness,

$$Re_\theta = Re_e\,\theta \qquad (4.15)$$

are shown in figure 30. Note that the momentum thickness and the displacement thickness considered in the above formulae are calculated from $\theta = \int_{y_w}^{y_e} (\rho u)/(\rho_e u_e)(1 - u/u_e)\mathrm{d}y$, and $\delta^* = \int_{y_w}^{y_e} 1 - (\rho u)/(\rho_e u_e)\mathrm{d}y$, respectively. The shape factor development in figure 30(*a*) shows similar features as the skin friction coefficient and Stanton number. It first decreases from the laminar value and then rises towards the laminar value before dropping again to a lower value as the boundary layer transitions to turbulence. The shape factor curves from all three cases can be seen to feature similar characteristics. The distribution of Reynolds number based on the momentum
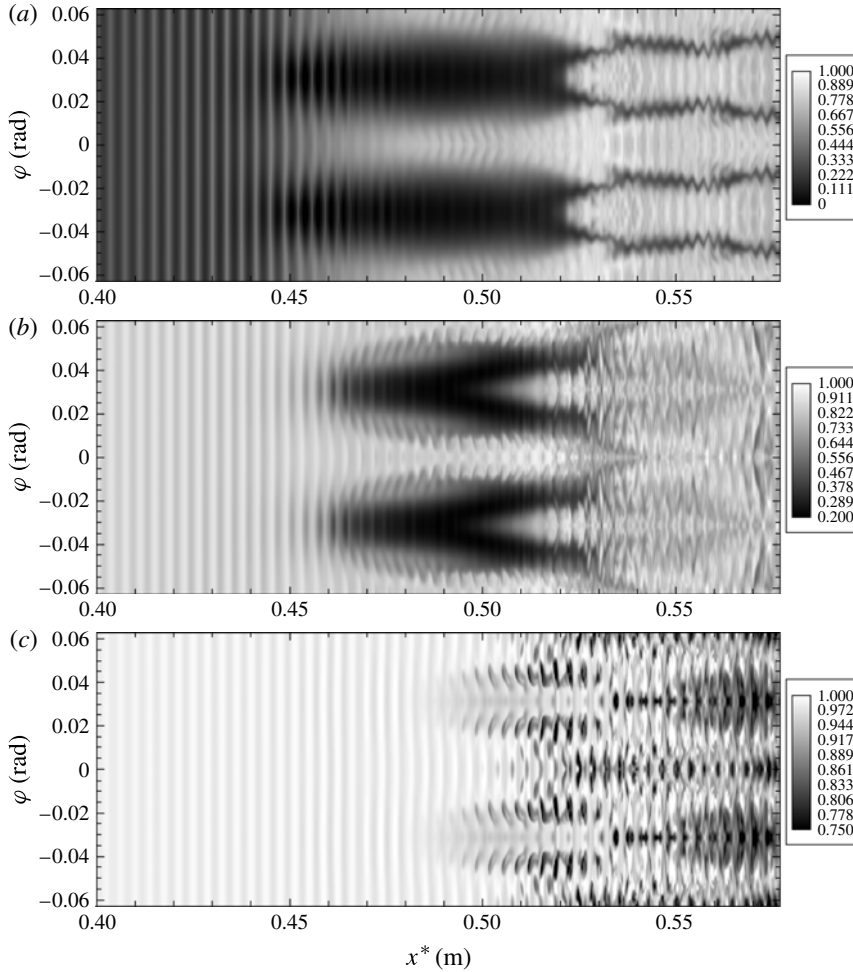
FIGURE 25. Contours of the instantaneous streamwise velocity in the x–φ plane for three wall-normal positions from CFUND 1: (*a*) $y^* = 0.35$ mm; (*b*) $y^* = 1.20$ mm; and (*c*) $y^* = 2.0$ mm.

thickness (see figure 30*b*), however, does not exhibit the trend observed for the shape factor (and also for skin friction and Stanton number). It initially follows the laminar curve up to $x^* \sim 0.42$ m and then increases monotonically to its highest value of $Re_\theta \sim 2500$ close to the end of the computational domain.

More insight into how far transition has progressed can be gained from the time-averaged streamwise velocity profiles plotted in wall coordinates. Here, the streamwise velocity is rescaled with the friction velocity,

$$u^+ = \frac{u}{u_\tau} \sqrt{Re}, \quad u_\tau = \sqrt{\frac{\tau_w}{\rho_w}}, \tag{4.16}$$

and the wall-normal coordinate is renormalized by

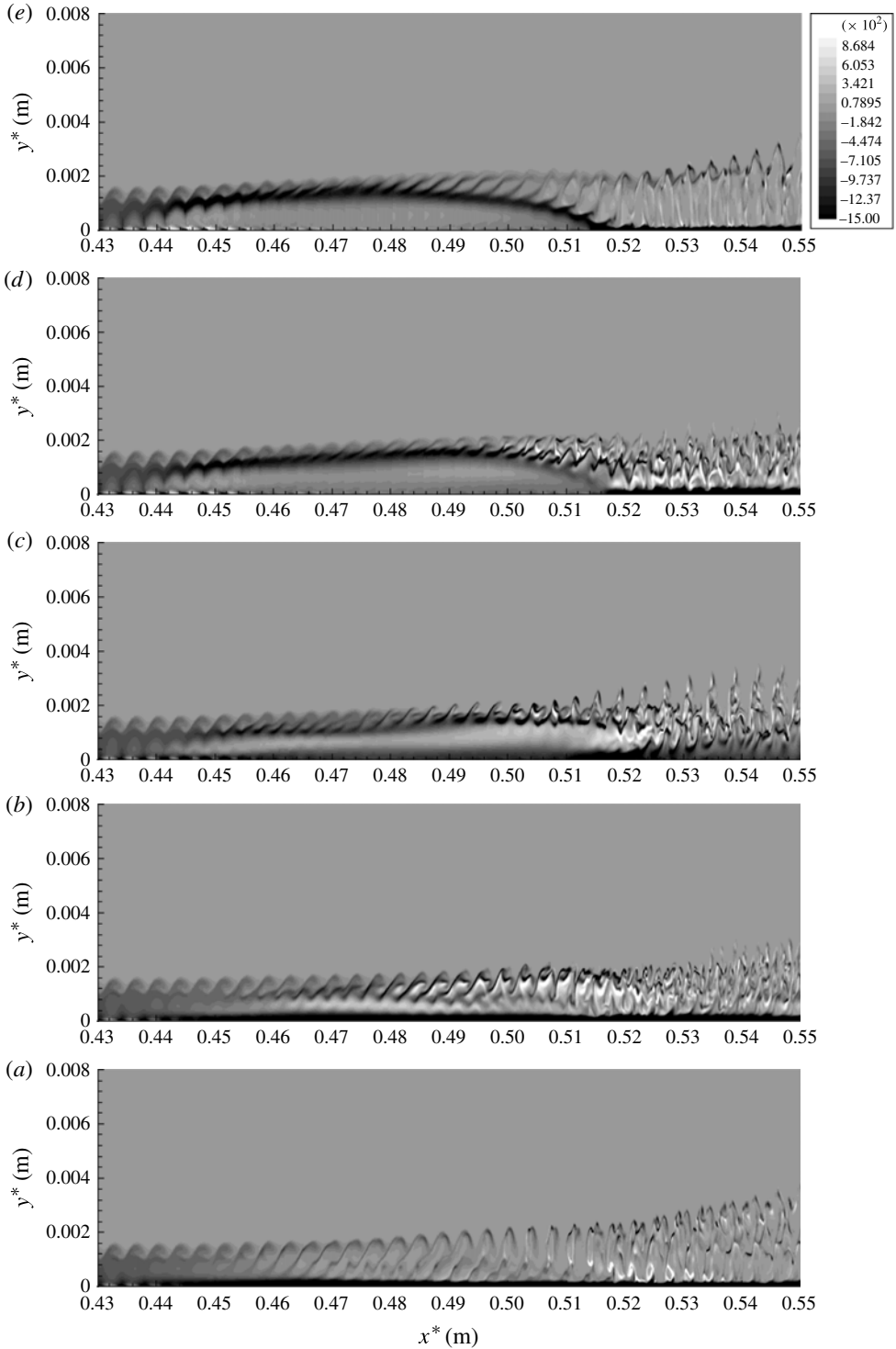$$y^+ = y \frac{\rho u_\tau}{\mu} \sqrt{Re}. \tag{4.17}$$

FIGURE 26. Contours of the instantaneous spanwise vorticity in the *x*–*y* plane for five azimuthal positions from CFUND 1. (*a*) $\varphi = 0$; (*b*) $\varphi = 0.0078$; (*c*) $\varphi = 0.0157$; (*d*) $\varphi = 0.0235$ and (*e*) $\varphi = 0.0314$ (from bottom to top). All plots have the same contour levels.
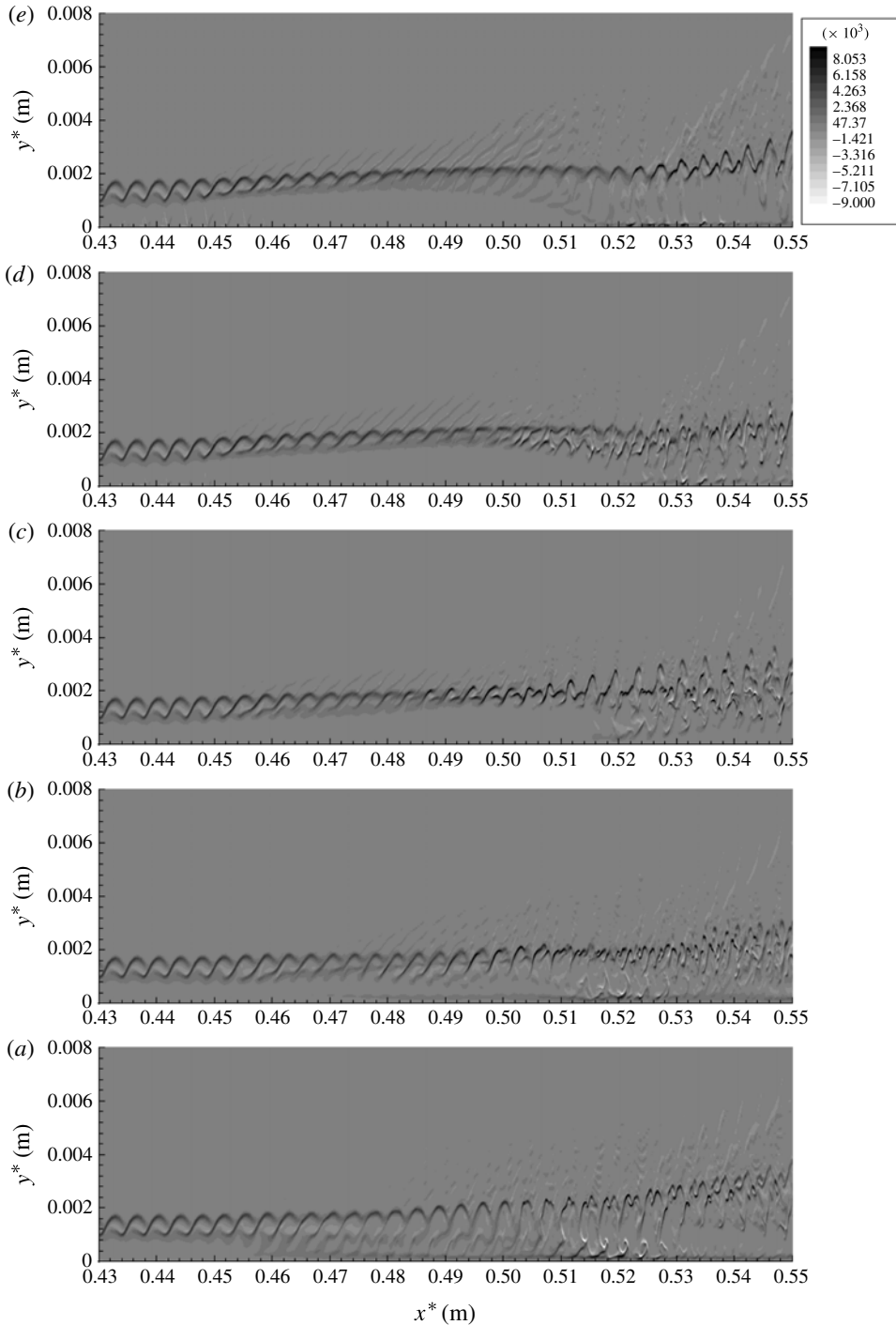
FIGURE 27. Contours of the instantaneous wall normal density gradient in the x–y plane for five azimuthal positions from CFUND 1. (*a*) $\varphi = 0$, (*b*) $\varphi = 0.0078$, (*c*) $\varphi = 0.0157$, (*d*) $\varphi = 0.0235$ and (*e*) $\varphi = 0.0314$ (from bottom to top). All plots have the same contour levels.
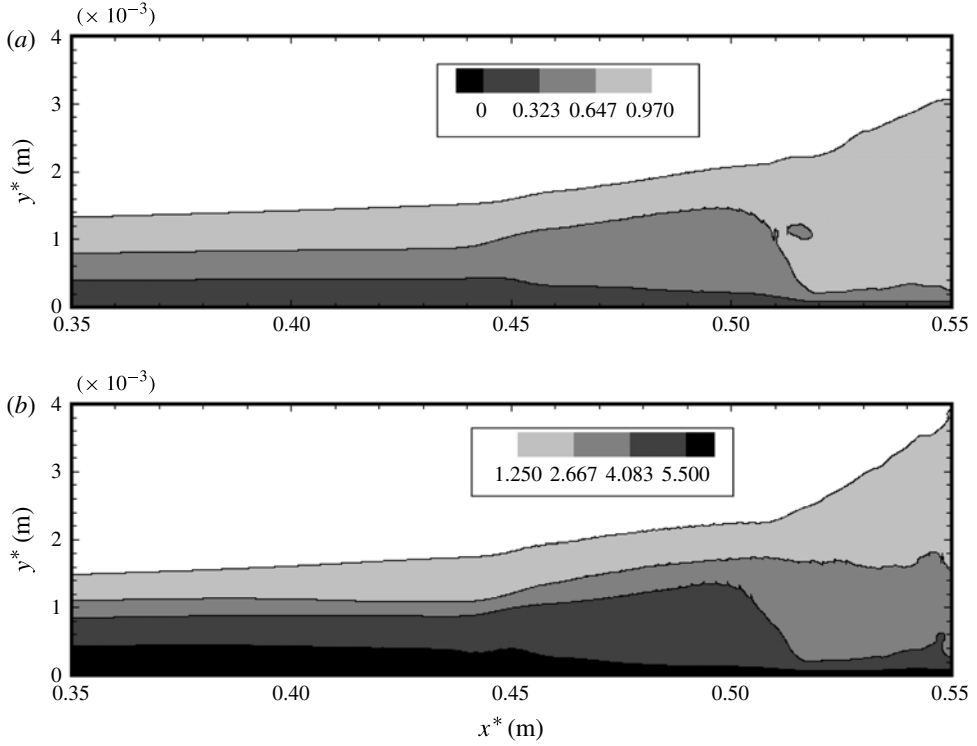
FIGURE 28. Contours of (*a*) the mean (in time and azimuthal direction) streamwise velocity and (*b*) the mean temperature from CFUND 1.
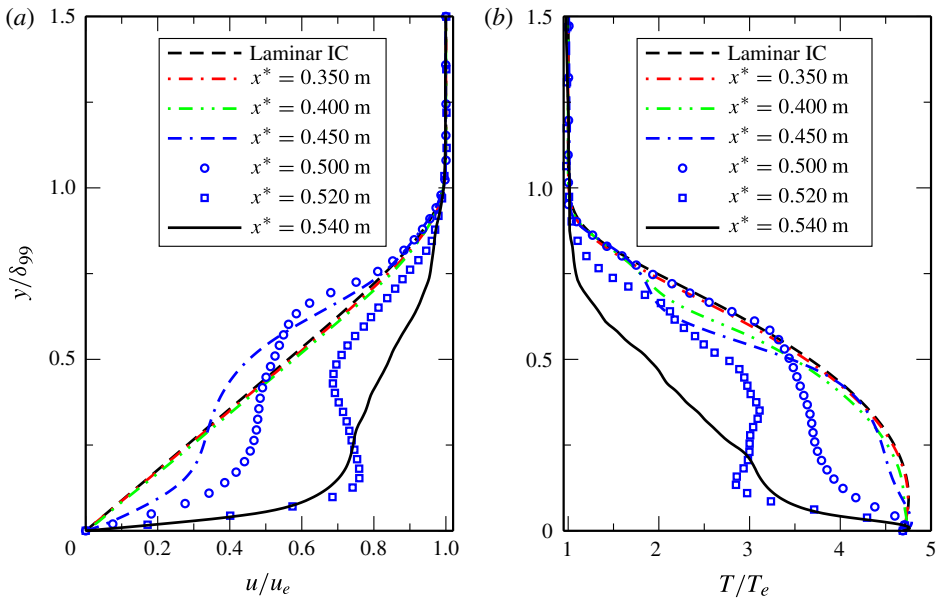

FIGURE 29. (Colour online) Selected wall-normal mean (*a*) streamwise velocity and (*b*) temperature profiles from CFUND 1.
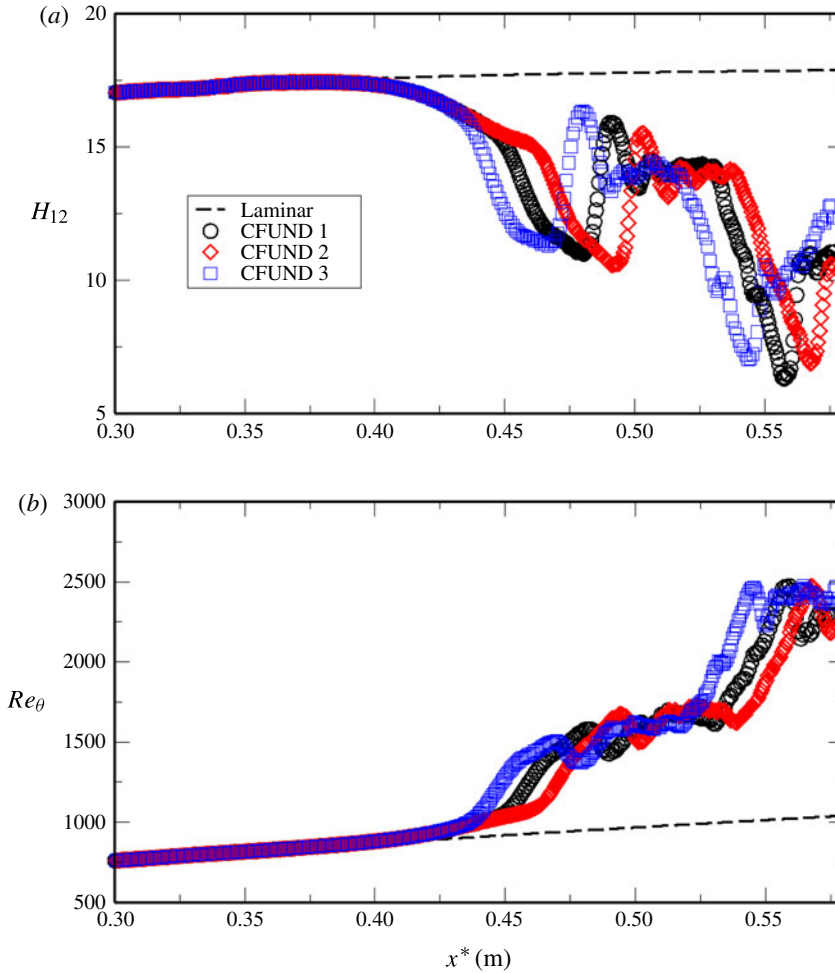
FIGURE 30. (Colour online) Downstream development of (*a*) the shape factor and (*b*) the Reynolds number based on momentum thickness.

Furthermore, for compressible flow the velocity is typically transformed using the van Driest transformation,

$$u_c^+ = \int_0^{u^+} \sqrt{\frac{T_w}{T}} \, \mathrm{d}u^+. \tag{4.18}$$

The transformed velocity profiles corresponding to several streamwise positions are shown in figure 31. Note that the dotted lines represent the theoretical curves for the linear sublayer and the logarithmic overlap region,

$$u^+ = y^+, \quad u^+ = \frac{1}{\kappa} \ln \left(y^+ \right) + C, \tag{4.19}$$

where $\kappa = 0.41$ and $C = 5.2$. For a location upstream of the transition onset location ($x^* \sim 0.35$ m), the velocity profile looks like a laminar profile. For locations close to the peak in the skin friction ($x^* = 0.54$ m), the turbulent log-layer shape is approached. This indicates that the flow is starting to become fully turbulent.
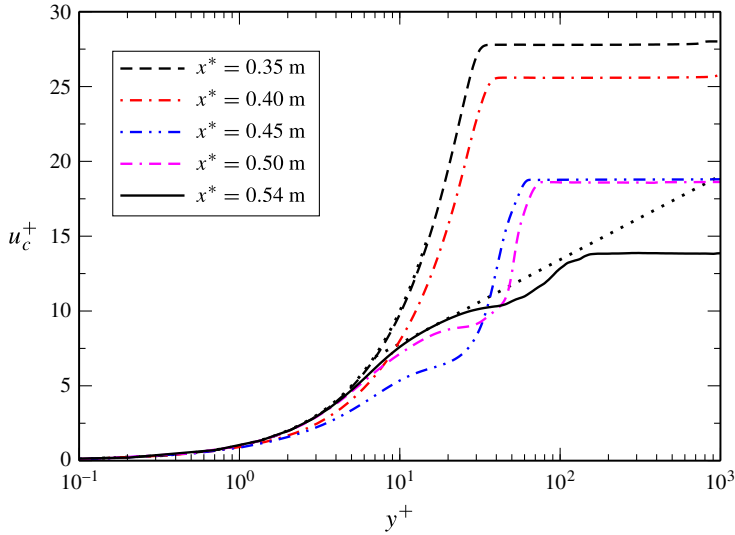
FIGURE 31. (Colour online) van-Driest-transformed streamwise velocity profiles normalized with the friction velocity for different streamwise positions obtained from the fundamental breakdown simulation CFUND 1. For streamwise position close to the peak in the skin friction ($x^* = 0.54$ m), the van-Driest-transformed velocity approaches the theoretical curves. The dotted lines indicate the linear sublayer and the law of the wall.

The state of the transition process can also be estimated using the energy spectra. For a spatial simulation typically both the time-averaged azimuthal wavenumber spectra and the azimuthal-averaged frequency spectra for different downstream positions are employed (see figures 32 and 33),

$$E(k_\varphi, j) = \frac{1}{N_t} \sum_{i=1}^{N_t} \overline{\phi}^2(i, j, k_\varphi), \quad \text{and} \quad E(\omega, j) = \frac{1}{N_\varphi} \sum_{k=1}^{N_\varphi} \overline{\phi}^2(\omega, j, k), \quad (4.20a,b)$$

where ϕ is the place holder for the velocity components. The indices j and k represent a grid point in the wall-normal and azimuthal direction, whereas i is the index for the time steps over which the average is performed; k_φ and ω denote the azimuthal wavenumber and the frequency, respectively. Furthermore, N_t and N_φ are the number of time steps and points over which the average is performed. The wall-normal position where the spectra are extracted is $y^* = 1.0$ mm. The rate of the energy decay for the range of wavenumbers in which neither the large eddies nor the small eddies have an influence on the spectrum (inertial subrange) can be predicted on theoretical grounds as $E \sim k_\varphi^{-5/3}$ (Weizäcker 1948). This theoretical behaviour is indicated by the red dashed lines in figure 32. Also indicated with blue dash-dotted lines is the decay according to $E \sim k_\varphi^{-7}$ at the high-wavenumber end of the spectrum as predicted by Heisenberg (1948). In figure 32, the time-averaged energy spectra are plotted versus the azimuthal wavenumber for streamwise velocity. For all three streamwise positions considered, the spectra agree well with the theoretically predicted decay rates for the inertial subrange and the high-wavenumber end of the spectra. As the flow transitions from laminar to transitional to turbulent, energy is transported from the base flow to large scales and then to smaller and smaller scales. This trend can be observed in the energy spectra presented in figure 32. In figure 33, the azimuthal-averaged energy
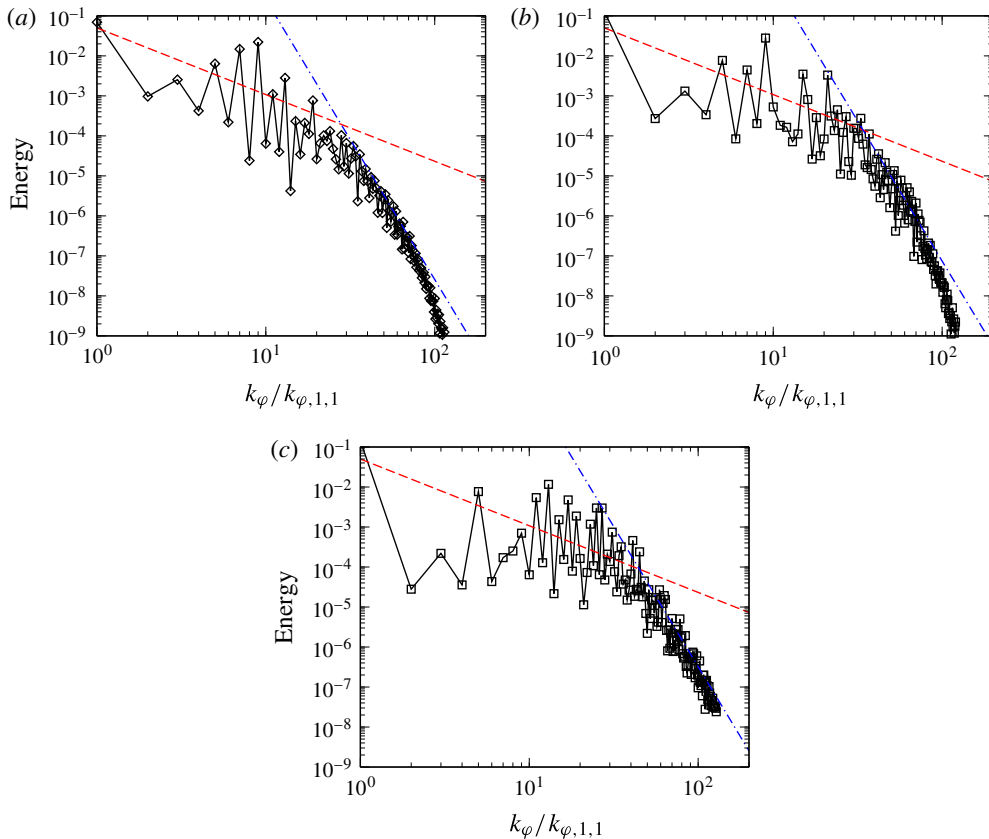
FIGURE 32. (Colour online) Energy spectra versus k_φ for streamwise velocity at (*a*) $x^* = 0.52$ m; (*b*) $x^* = 0.54$ m and (*c*) $x^* = 0.56$ m from CFUND 1. The red and blue lines indicate the theoretical estimate for the decay of the energy spectrum: $E \sim k_\varphi^{-5/3}$ (red line) and $E \sim k_\varphi^{-7}$ (blue line).

spectra are plotted versus the frequency. For all three streamwise positions, the azimuthally averaged spectrum experience a decay as predicted by theory. Therefore, based on these spectra, one can conclude that the boundary layer is close to fully turbulent at the end of the computational domain.

5. Conclusion

Direct numerical simulations were performed to investigate transition in a sharp cone boundary layer at Mach 6. In preceeding investigations we have explored which nonlinear mechanisms for a hypersonic cone boundary layer are present in a broad-band disturbance environment, or a 'natural transition' scenario, by using wavepacket disturbances. These investigations have indicated that second-mode fundamental resonance may be a relevant nonlinear mechanism for a sharp cone boundary layer at Mach 6 for the conditions of the Purdue experiments. However, a nonlinear mechanism is only relevant for the transition process if it can lead to a complete breakdown to turbulence and to fully developed turbulent flow. Hence, in order to answer this question, in this paper we explore the role of fundamental resonance or (K-type) breakdown for a cone boundary layer Mach 6.
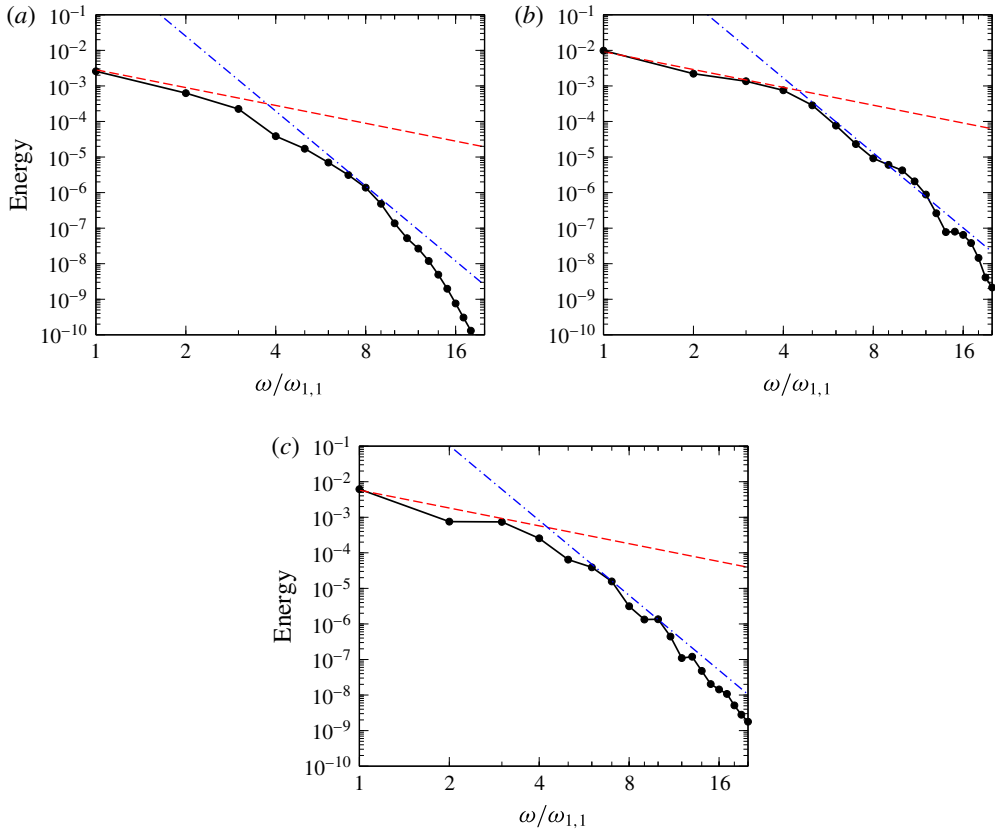
FIGURE 33. (Colour online) Energy spectra versus ω for streamwise velocity at (*a*) $x^* = 0.52$ m; (*b*) $x^* = 0.54$ m and (*c*) $x^* = 0.56$ m from CFUND 1. The red and blue lines indicate the theoretical estimate for the decay of the energy spectrum: $E \sim \omega^{-5/3}$ (red line) and $E \sim \omega^{-7}$ (blue line).

First, a parameter study was performed to determine the most relevant cases by performing several small- and medium-scale simulations. Subsequently, a set of highly resolved 'controlled' fundamental (K-type) breakdown simulations was performed, using the disturbance parameters that resulted in the strongest secondary growth for fundamental resonance. In these simulations the skin friction coefficient initially follows the laminar curve and then increases towards the theoretical turbulent curve. However, farther downstream the skin friction drops down close to the laminar values before rising steeply again and eventually overshooting the turbulent curve. A closer look at the streamwise development of the disturbance waves revealed that the initial rise in skin friction is caused by the large-amplitude primary wave (1, 0). The first peak in the skin friction roughly corresponds to the streamwise location where the primary wave (1, 0) attains 'nonlinear saturation'. As the primary wave starts to decay following the 'nonlinear saturation', due to mean flow deformation, the skin friction decreases strongly. Then, finally, a steep rise in skin friction and a skin friction overshoot over the theoretical skin friction for the turbulent boundary layer occurs when all higher modes experience strong nonlinear amplification.

In the fundamental breakdown simulations presented in this paper, nonlinear interactions lead to the generation of strong stationary streamwise vortex modes, which

manifest themselves as streamwise 'hot' streaks in visualizations of the skin friction and the wall-normal temperature gradient. Such streamwise streaks were also observed for a flared cone at Mach 6 in the experiments at Purdue University. Therefore, it is conjectured that second-mode fundamental breakdown could have played a role in the 'natural' unforced transition experiments at Purdue University. Furthermore, the controlled transition simulations presented in this paper have demonstrated that fundamental breakdown can lead to a fully developed turbulent boundary layer and, therefore, may be a viable path for transition to turbulence in hypersonic boundary layers at Mach 6.

Acknowledgements

REFERENCES

ALBA, C. R., CASPER, K. M., BERESH, S. J. & SCHNEIDER, S. P. 2010 Comparison of experimentally measured and computed second-mode disturbances in hypersonic boundary-layers. *AIAA Paper* 2010-0897.

BALAKUMAR, P. & MALIK, M. R. 1992 Discrete modes and continuous spectra in supersonic boundary layers. *J. Fluid Mech.* **239**, 631–656.

BALSARA, D. S. & SHU, C.-W. 2000 Monotonicity preserving weighted essentially non-oscillatory schemes with increasingly high-order of accuracy. *J. Comput. Phys.* **160**, 405–452.

BECKWITH, I. E., CREEL, T. R., CHEN, F.-J. & KENDALL, J. M. 1983 Free stream noise and transition measurements in a Mach 3.5 pilot quiet tunnel. *AIAA Paper* 1983-0042.

BERRIDGE, D., CHOU, A., WARD, C., STEEN, L., GILBERT, P., JULIANO, T., SCHNEIDER, S. & GRONVALL, J. 2010 Hypersonic boundary-layer transition experiments in a Mach 6 quiet tunnel. *AIAA Paper* 2010-1061.

BERRY, S. A., HAMILTON, H. H. & WURSTER, K. E. 2006 Effect of computational method on discrete roughness correlations for shuttle orbiter. *J. Spacecr. Rockets* **43** (4), 842–852.

BERRY, S. A. & HORVARTH, T. J. 2008 Discrete roughness transition for hypersonic flight vehicles. *J. Spacecr. Rockets* **45** (2), 216–227.

BOUNTIN, D., SHIPLYUK, A. & MASLOV, A. 2008 Evolution of nonlinear processes in a hypersonic boundary layer on a sharp cone. *J. Fluid Mech.* **611**, 427–442.

BOUNTIN, D. A., SHIPLYUK, A. N. & SIDORENKO, A. A. 1999 Experimental investigations of disturbance development in the hypersonic boundary layer on a conical model. In *Laminar-Turbulent Transition* (ed. H. F. Fasel & W. S. Saric), pp. 475–480. Springer.

CANUTO, C., HUSSAINI, M., QUATERONI, A. & ZANG, T. 1988 *Spectral Methods in Fluid Dynamics*. Springer.

CASPER, K. M., BERESH, S. J., HENFLING, J. F., SPILLERS, R. W., PRUETT, B. & SCHNEIDER, S. P. 2009 Hypersonic wind-tunnel measurements of boundary-layer pressure fluctuations. *AIAA Paper* 2009-4054.

CHEN, F.-J., MALIK, M. R. & BECKWITH, I. E. 1988 Comparison of boundary-layer transition on a cone and flat plate at Mach 3.5. *AIAA Paper* 1988-0411.

CHEN, F. J., MALIK, M. R. & BECKWITH, I. E. 1989 Boundary-layer transition on a cone and flat plate at Mach 3.5. *AIAA J.* **27**, 687–693.

CHOKANI, N. 1999 Nonlinear spectral dynamics of hypersonic laminar boundary layer flow. *Phys. Fluids* **11** (12), 3846–3851.

CHOKANI, N. 2005 Nonlinear evolution of Mack modes in a hypersonic boundary layer. *Phys. Fluids* **17**, 014102.

DEMETRIADES, A. 1960 An experiment on the stability of hypersonic laminar boundary layers. *J. Fluid Mech.* **7**, 385–396.

DEMETRIADES, A. 1974 Hypersonic viscous flow over a slender cone, part: III: laminar instability and transition. *AIAA Paper* 1974-0535.

DEMETRIADES, A. 1977 Boundary layer instability observations at Mach number 7. *Trans. ASME: J. Appl. Mech.* **99**, 7–10.

DEMETRIADES, A. 1978 New experiments on hypersonic boundary layer stability including wall temperature effects. In *Proceedings of the 1978 Heat Transfer and Fluid Mechanics Institute*, pp. 39–54. Stanford University Press.

VAN DRIEST, E. 1952 Turbulent boundary layer on a cone in a supersonic flow at zero angle of attack. *J. Aero. Sci.* **19**, 55–57.

EISSLER, W. 1995 Numerische Untersuchungen zum laminar-turbulenten Strömungsumschlag in Überschallgrenzschichten. PhD thesis, Universität Stuttgart.

EISSLER, W. & BESTEK, H. 1996 Spatial numerical simulations of linear and weakly nonlinear wave instabilities in supersonic boundary layers. *Theor. Comput. Fluid Dyn.* **8**, 219–235.

FASEL, H. F. 1990 Numerical simulation of instability and transition in boundary layer flows. In *Laminar-Turbulent Transition* (ed. D. Arnal & R. Michel), pp. 587–597. Springer.

FASEL, H. F. & KONZELMANN, U. 1990 Non-parallel stability of a flat-plate boundary layer using the complete Navier–Stokes equations. *J. Fluid Mech.* **221**, 311–347.

FASEL, H., THUMM, A. & BESTEK, H. 1993 Direct numerical simulation of transition in supersonic boundary layer: oblique breakdown. In *Transitional and Turbulent Compressible Flows* (ed. L. D. Kral & T. A. Zang), FED, vol. 151, pp. 77–92. ASME.

FEDOROV, A. V. 2011 Transition and stability of high-speed boundary layers. *Annu. Rev. Fluid Mech.* **43**, 79–95.

FERZIGER, J. H. 1998 *Numerical Methods for Engineering Application*, 2nd edn. Wiley-Interscience.

FEZER, A. & KLOKER, M. 2001 Grenzschichtumschlag bei Überschallströmung. *Sonderforschungsbericht* 259. DFG.

FISHER, D. F. & DOUGHERTY, N. S. 1982 In-flight transition measurement on a 10° cone at Mach numbers from 0.5 to 2.0. *TP* 1971. NASA.

GASPERAS, G. 1987 The stability of the compressible boundary layer on a sharp cone at zero angle of attack. *AIAA Paper* 1987-0494.

GASTER, M. 1974 On the effects of boundary-layer growth on flow stability. *J. Fluid Mech.* **66**, 465–480.

GROSS, A. & FASEL, H. F. 2008 High-order accurate numerical method for complex flows. *AIAA J.* **46**, 204–214.

GROSS, A. & FASEL, H. F. 2010 Numerical investigation of supersonic flow for axisymmetric cones. *Maths Comput. Simul.* **81**, 133–142.

HANEY, J. W. 1983 Orbiter entry heating lessons learned from development flight test program. In *Shuttle Performance: Lessons Learned, Part 2* (ed. J. P. Arrington & J. J. Jones), pp. 719–751, NASA-CP-2283.

HARRIS, P. J. 1997 Numerical investigation of transitional compressible plane wakes. PhD thesis, The University of Arizona.

HEISENBERG, W. 1948 Zur statistischen Theorie der Turbulenz. *Z. Phys.* **124**, 628–657.

HERBERT, T. 1988 Secondary instability of boundary layers. *Annu. Rev. Fluid Mech.* **20**, 487–526.

HORVATH, T. J., BERRY, S. A., HOLLIS, B. R., CHANG, C.-L. & SINGER, B. A. 2002 Boundary layer transition on slender cones in conventional and low disturbance Mach 6 wind tunnels. *AIAA Paper* 2002-2743.

HUNT, J. C. R., WRAY, A. A. & MOIN, P. 1988 Eddies, streams, and convergence zones in turbulent flows. In *Proceedings of the 1988 Summer Research Program, Center for Turbulence Research, Stanford University*, pp. 193–208.

HUSMEIER, F. & FASEL, H. F. 2007 Numerical investigations of hypersonic boundary layer transition for circular cones. *AIAA Paper* 2007-3843.

KACHANOV, YU. S. 1994 Physical mechanisms of laminar boundary-layer transition. *Annu. Rev. Fluid Mech.* **26**, 411–482.

KENDALL, J. M. 1975 Wind tunnel experiments relating to supersonic and hypersonic boundary-layer transition. *AIAA J.* **13**, 290–299.

LACHOWICZ, J. T., CHOKANI, N. & WILKINSON, S. P. 1996 Boundary-layer stability measurements in a hypersonic quiet tunnel. *AIAA J.* **34** (12), 2496–2500.

LAIBLE, A. C. 2011 Numerical investigation of boundary-layer transition for cones at Mach 3.5 and 6.0. PhD thesis, University of Arizona.

LAIBLE, A. C., MAYER, C. S. J. & FASEL, H. F. 2008 Numerical investigation of supersonic transition for a circular cone at Mach 3.5. *AIAA Paper* 2008-4397.

LAIBLE, A. C., MAYER, C. S. J. & FASEL, H. F. 2009 Numerical investigation of transition for a cone at Mach 3.5: oblique breakdown. *AIAA Paper* 2009-3557.

VAN LEER, B. 1982 Flux-vector splitting for the Euler equations. In *International Conference on Numerical Methods in Fluid Dynamics*, vol. 170, pp. 507–512. Springer.

MACK, L. M. 1965 Computation of the stability of the laminar compressible boundary layer. In *Methods of Comp. Physics* (ed. B. Alder, S. Fernbach & M. Rotenberg), vol. 4, pp. 247–299. Academic.

MACK, L. M. 1969 Boundary-layer stability theory. Internal Document 900-277. Jet Propulsion Laboratory, Pasadena, California.

MACK, L. M. 1975 Linear stability theory and the problem of supersonic boundary-layer transition. *AIAA J.* **13**, 278–289.

MACK, L. M. 1984 Boundary-layer linear stability theory. *AGARD Report* 709. Advisory Group for Aerospace Research and Development.

MACK, L. M. 1987 Stability of axisymmetric boundary layers on sharp cones at hypersonic Mach numbers. *AIAA Paper* 1987-1413.

MALIK, M. R. 1984 Instability and transition in supersonic boundary layers. In *Laminar Turbulent Boundary Layers; Proceedings of the Energy Sources Technology Conferences* (ed. E. M. Uram & H. E. Weber), pp. 139–147. ASME.

MANGLER, W. 1948 Zusammenhang zwischen ebenen und rotationssymmetrischen Grenzschichten in kompressiblen Flüssigkeiten. *Z. Angew. Math. Mech.* **28** (4), 97–103.

MASLOV, A. A., SHIPLYUK, A. N., BOUNTIN, D. A. & SIDORENKO, A. A. 2006 Mach 6 boundary-layer stability experiments on sharp and blunted cones. *J. Spacecr. Rockets* **43** (1), 71–76.

MASLOV, A. A., SHIPLYUK, A. N., SIDORENKO, A. A. & ARNAL, D. 2001 Leading-edge receptivity of a hypersonic boundary layer on a flat plate. *J. Fluid Mech.* **426**, 73–94.

MEITZ, H. & FASEL, H. F. 2000 A compact-difference scheme for the Navier–Stokes equations in vorticity-velocity formulation. *J. Comput. Phys.* **157**, 371–403.

POINSOT, T. J. & LELE, S. K. 1992 Boundary conditions for direct simulations of compressible viscous flows. *J. Comput. Phys.* **101**, 104–129.

PRUETT, C. D. & CHANG, C.-L. 1995 Spatial direct numerical simulation of high-speed boundary-layer flows. Part II: transition on a cone in Mach 8 flow. *Theor. Comput. Fluid Dyn.* **7**, 397–424.

PRUETT, C. D. & CHANG, C.-L. 1998 Direct numerical simulation of hypersonic boundary-layer flow on a flared cone. *Theor. Comput. Fluid Dyn.* **11**, 49–67.

PRUETT, C. D., ZANG, T. A., CHANG, C.-L. & CARPENTER, M. H. 1995 Spatial direct numerical simulation of high-speed boundary-layer flows. Part I: algorithmic considerations and validation. *Theor. Comput. Fluid Dyn.* **7**, 49–76.

ROY, C. J. & BLOTTNER, F. G. 2006 Review and assessment of turbulence models for hypersonic flows. *Prog. Aerosp. Sci.* **42**, 469–530.

SARIC, W. S. & NAYFEH, A. H. 1975 Nonparallel stability of boundary layer flows. *Phys. Fluids* **18**, 945–950.

SCHNEIDER, S. P. 2001 Effects of high-speed tunnel noise on laminar-turbulent transition. *J. Spacecr. Rockets* **38** (3), 323–333.

SCHNEIDER, S. P. 2004 Hypersonic laminar-turbulent transition on circular cones and scramjet forebodies. *Prog. Aerosp. Sci.* **40**, 1–50.

SHIPLYUK, A. N., BOUNTIN, D. A., MASLOV, A. A. & CHOKANI, N. 2003 Nonlinear mechanisms of the initial stage of laminar-turbulent transition at hypersonic velocities. *J. Appl. Mech. Tech. Phys.* **44** (5), 654–659.

SIVASUBRAMANIAN, J. & FASEL, H. F. 2010 Numerical investigation of boundary-layer transition initiated by a wavepacket for a cone at Mach 6. *AIAA Paper* 2010-0900.

SIVASUBRAMANIAN, J. & FASEL, H. F. 2011 Numerical investigation of laminar-turbulent transition in a cone boundary layer at Mach 6. *AIAA Paper* 2011-3562.

SIVASUBRAMANIAN, J. & FASEL, H. F. 2012a Growth and breakdown of a wavepacket into a turbulent spot in a cone boundary layer at Mach 6. *AIAA Paper* 2012-0085.

SIVASUBRAMANIAN, J. & FASEL, H. F. 2012b Nonlinear stages of transition and breakdown in a boundary layer on a sharp cone at Mach 6. *AIAA Paper* 2012-0087.

SIVASUBRAMANIAN, J. & FASEL, H. F. 2014 Numerical investigation of the development of three-dimensional wavepackets in a sharp cone boundary layer at Mach 6. *J. Fluid Mech.* **756**, 600–649.

SIVASUBRAMANIAN, J., MAYER, C. S. J., LAIBLE, A. C. & FASEL, H. F. 2009 Numerical investigation of wavepackets in a hypersonic cone boundary layer at Mach 6. *AIAA Paper* 2009-3560.

STETSON, K. F. & KIMMEL, R. L. 1992 On hypersonic boundary-layer stability. *AIAA Paper* 1992-0737.

STETSON, K. F. & KIMMEL, R. L. 1993 On the breakdown of a hypersonic laminar boundary layer. *AIAA Paper* 1993-0896.

STETSON, K. F., THOMPSON, E. R., DONALDSON, J. C. & SILER, L. G. 1983 Laminar boundary layer stability experiments on a cone at Mach 8. Part I: sharp cone. *AIAA Paper* 1983-1761.

STETSON, K. F., THOMPSON, E. R., DONALDSON, J. C. & SILER, L. G. 1984 Laminar boundary layer stability experiments on a cone at Mach 8. Part II: blunt cone. *AIAA Paper* 1984-0006.

STETSON, K. F., THOMPSON, E. R., DONALDSON, J. C. & SILER, L. G. 1985 Laminar boundary layer stability experiments on a cone at Mach 8. Part III: sharp cone at angle of attack. *AIAA Paper* 1985-0492.

STETSON, K. F., THOMPSON, E. R., DONALDSON, J. C. & SILER, L. G. 1986 Laminar boundary layer stability experiments on a cone at Mach 8. Part IV: on unit Reynolds number and environmental effects. *AIAA Paper* 1986-1087.

STETSON, K. F., THOMPSON, E. R., DONALDSON, J. C. & SILER, L. G. 1989 Laminar boundary layer stability experiments on a cone at Mach 8. Part V: tests with a cooled model. *AIAA Paper* 1989-1895.

THUMM, A. 1991 Numerische Untersuchungen zum laminar-turbulenten Strömungsumschlag in transsonischen Grenzschichtströmungen. PhD thesis, Universität Stuttgart.

TUMIN, A. 2007 Three-dimensional spatial normal modes in compressible boundary layers. *J. Fluid Mech.* **586**, 295–322.

WARD, C., WHEATON, B., CHOU, A., BERRIDGE, D., LETTERMAN, L., LUERSEN, R. & SCHNEIDER, S. 2012 Hypersonic boundary-layer transition experiments in the Boeing/AFOSR Mach 6 quiet tunnel. *AIAA Paper* 2012-0282.

WEIZÄCKER, C. F. v. 1948 Das Spektrum der Turbulenz bei großen Reynoldsschen Zahlen. *Z. Phys. A Hadrons Nuclei* **124**, 614–627.

WHITE, F. M. 2006 *Viscous Fluid Flow*. McGraw-Hill.

ZHONG, X. 1998 High-order finite-difference schemes for numerical simulation of hypersonic boundary-layer transition. *J. Comput. Phys.* **144**, 662–709.

ZHONG, X. 2001 Leading-edge receptivity to free-stream disturbance waves for hypersonic flow over a parabola. *J. Fluid Mech.* **441**, 315–367.

ZHONG, X. & TATINENI, M. 2003 High-order non-uniform grid schemes for numerical simulation of hypersonic boundary-layer stability and transition. *J. Comput. Phys.* **190**, 419–458.